

LIGHT SCATTER BASED LABEL-FREE ASSESSMENT OF
MITOCHONDRIAL MORPHOLOGY AND DYNAMICS

By

MOHAMMAD NASER

A dissertation submitted to the

School of Graduate Studies

Rutgers, The State University of New Jersey

In partial fulfillment of the requirements

For the degree of

Doctor of Philosophy

Graduate Program in Biomedical Engineering

Written under the direction of

Nada N. Boustany

And approved by

New Brunswick, New Jersey

October, 2018

ABSTRACT OF THE DISSERTATION

Light Scatter based Label-free Assessment of Mitochondrial Morphology and Dynamics

by

Mohammad Naser

Dissertation Director
Dr. Nada N. Boustany

Live-cell imaging has become increasingly important to the scientific community as researchers aim to understand the morphology and dynamics of the subcellular structures. Specifically, mitochondrial morphology under healthy and pathologic conditions is an emerging area of interest, with applications in neuroprotective drug discovery amongst many. Fluorescent dyes act as the current biological gold standard for visualizing organelles in live-cell imaging, yet they have been shown to cause adverse effects on subcellular functions, prompting the development of alternate, “label-free”, methods of imaging. By employing Optical Scatter Imaging (OSI), which is based on optical Fourier filtering where scattered light is filtered by the hardware using size and orientation sensitive Gabor filters, images can be acquired label-free and processed to extract morphometric data. As groundwork for developing a label-free method for probing mitochondria, we first demonstrated that optical scatter imaging with principal component analysis (PCA) can classify apoptosis-competent Bax/Bak-expressing, and apoptosis resistant Bax/Bak-null immortalized baby mouse kidney (iBMK) cells without the use of fluorescent labels. Furthermore, in Bovine Aortic Endothelial Cells (BAEC), a different cell type, we revealed that label-free Optical Scatter Imaging (OSI) can be combined with digital segmentation to create dynamic subcellular masks. These masks

can be used to extract the “orientedness” of organelles, which corresponds to an organelle’s degree of orientation, allowing the quantification of organelle morphology during cell injury induced by calcium overload. In order to optimize this label free imaging and processing method for neuronal mitochondria, we applied a size-encoding parameter, “Smax”. All in all, we have developed different approaches to detect and quantify morphological changes associated with mitochondria and other organelles in three different cell-types and we have compared the results with a fluorescent data. This ultimately implies that our label-free imaging technique can be modified for use in many cell types, enabling numerous possible research applications in organelle visualization.

ACKNOWLEDGEMENT

My PhD is by far the most exciting journey I have ever endeavored, as well as the most challenging, both mentally and physically. From experiencing the bitter winter to getting myself familiarized with a completely different field of studies – this journey has put me into a variety of situations which would have been impossible to cope without help from some kind souls.

First of all, I would like to thank my advisor Dr. Nada Boustany for giving me the opportunity to work in her lab. You are one of the best mentors I had, and I aspire to follow the strong example of hard work and attention to detail that you have set for me. Thanks for your guidance and patience. Another key person is Dr. Rene Schloss whose continuous support kept me on track and helped me to finish on time. Thanks to Dr. Bonnie Firestein for generously supplying neurons for my experiments. Thank you Dr. Mathieu Petitjean for your mentorship and for your insights into the biomedical imaging industry. Also, I would like to thank Dr. Mark Pierce for your advice and time.

I really can't thank Ileana, Nazmul bhai and Nipun apu enough for their help throughout this journey. You all generously took time out of your personal lives to help me acclimate to life in America, and I owe so many of my successes to your kindness. I would like to thank my friend Shatila for being there for me with her wisdom, courage and care, which will even continue guiding me through difficult situations in life.

My fellow graduate students in BME have been indispensable to me along my journey, and I have both learned so much and shared so much with you all. Manjari, Harini, Rohit, Cosmas, Prakhar, Yoliem, Maria, Jack and Chris – you guys have been my “lab-mates”

from another lab. Thanks for telling me “You’ve got this” whenever I faced a road-block. A special thanks goes to the undergrads, Erin and Corey in my lab for helping me with the neuronal studies.

Workout and tennis have kept me sane for last two years and I would like to thank my bro-cum-trainer Nick and my tennis partner Ricky for their time and effort. You guys didn’t have to stick with me, still you did and I’m so much grateful for that.

Amartya, thanks for showing me what it takes to be an ideal graduate student. Had I not met you, I would have not known the true meaning of so many things I took for granted. During our brief encounter, you had introduced me to Richard Feynman, Roger Federer, Sam Manekshaw, Ruskin Bond, Hrishikesh Mukherjee and many others who will continue inspiring me forever.

My mom and aunt has been the driving force for my education. It is for their sacrifice I reached to this point in life and it is to them I dedicate this dissertation.

TABLE OF CONTENTS

Abstract.....	ii
Acknowledgement.....	iv
1 INTRODUCTION AND REVIEW OF RELATED WORK.....	1
1.1 Live-cell Imaging: current gold-standard.....	1
1.2 Live-cell Imaging with Optical Methods	1
1.2.1 Imaging Based on Elastic Scattering	2
1.2.2 Second Harmonic generation (SHG)	4
1.2.3 Two Photon Excitation Fluorescence (TPEF)	5
1.2.4 Brillouin Microscopy	5
1.2.5 Super-resolution Microscopy.....	6
1.2.6 Fourier Ptychography.....	7
1.3 Previous Work.....	7
2 LABEL-FREE CLASSIFICATION OF BAX/BAK EXPRESSING VS. DOUBLE-KNOCKOUT CELLS.....	12
2.1 Introduction	13
2.2 Materials and Methods.....	15
2.2.1 Cell preparation.....	15
2.2.2 Optical Scatter Imaging (OSI)	15
2.2.3 Image pre-processing	16
2.2.4 Principal Component Analysis (PCA).....	17
2.2.5 Linear Discriminant Analysis Classifier.....	19
2.2.6 Feature Selection Algorithm.....	20
2.3 Results	20
2.3.1 Representative DIC and dark field images	20
2.3.2 Feature extraction and detection of genetic mutation.....	21
2.4 Discussion	29
3 LABEL-FREE DYNAMIC SEGMENTATION AND MORPHOLOGICAL ANALYSIS OF SUBCELLULAR OPTICAL SCATTERERS.....	39
3.1 Introduction	40
3.2 Methods.....	42

3.2.1	Cell culture.....	42
3.2.2	Calcium treatment.....	42
3.2.3	Optical setup and image acquisition	43
3.2.4	Gabor filter design	44
3.2.5	Generating local energy and phase congruency (maximum moment) images	46
3.2.6	Generating Orientedness images.....	48
3.2.7	Image segmentation	48
3.3	Results	49
3.3.1	Cell images produced by the algorithm	49
3.3.2	Tracking subcellular organelles with dynamic masking.....	50
3.3.3	Effect of Jain’s multi-channel filtering approach	54
3.3.4	Aspect-ratio and Orientedness decrease upon injury.....	55
3.3.5	Texture-features can detect subcellular morphological dynamics induced by injury	56
3.4	Discussion	59
	Acknowledgements.....	64
	Appendix.....	65
4	LIGHT SCATTER BASED LABEL-FREE ASSESSMENT OF GLUTAMATE INDUCED EXCITOTOXICITY ON MITOCHONDRIAL DYNAMICS	67
4.1	Introduction	68
4.1.1	Role of glutamate.....	69
4.1.2	Role of calcium.....	69
4.1.3	Assessment of mitochondrial dynamics via imaging techniques	70
4.2	Methods.....	72
4.2.1	Cell culture and Transfection.....	72
4.2.2	Glutamate treatment.....	73
4.2.3	Image acquisition	73
4.2.4	Image processing	73
4.3	Results	74
4.3.1	Reporting change in organelle-size.....	74
4.3.2	Tracking organelle movement	76

4.4	Discussion	78
5	CONCLUSION & FUTURE DIRECTION.....	86

LIST OF FIGURES

- Figure 2-1 Principal component analysis (PCA) of the dark-field image stack at each Gabor filter period. For each Gabor filter period, each cell image is reshaped into a $1 \times 65,536$ vector yielding a $236 \times 65,536$ matrix in which each row represents a cell vector. PCA applied along the pixel dimension yields principal component vectors which are $65,536 \times 1$. Each principal component may be reshaped into an image matrix representing an “eigencell” for the data set at the Gabor filter period analyzed (Filter_i). Only the first principal component was kept, resulting in a total of 100 eigencell images corresponding to each Gabor filter period. 19
- Figure 2-2 Representative images of a Bax/Bak expressing (W2) cell A: Dark-field image showing the full field of view. The white rectangle indicates the region of the field that was also imaged by differential interference contrast (DIC) (B). C: Filtered images of the cell outlined by the yellow dotted line in Panels A and B are shown for several Gabor filters with varying periods, S , and orientation, j , of either 0° or 90° 22
- Figure 2-3 Representative images of a Bax/Bak double knockout (D3) cell. A: Dark-field image showing the full field of view. The white rectangle indicates the region of the field was also imaged by differential interference contrast (DIC) (B). C: Filtered images of the cell outlined by the yellow dotted line in Panels A and B are shown for several Gabor filters with varying periods, S , and orientation, j , of either 0° or 90° 23
- Figure 2-4 Representative eigencell images obtained at 8 different Gabor filter periods. Images taken with Gabor filter orientations at 0° and 90° degrees were averaged together at each Gabor filter period before performing the PCA. The color scale corresponds to the normalized values of the PC vectors from which the eigencell images were formed. 24
- Figure 2-5 Generation of the Feature Matrix for cell classification. The reshaped $236 \times 65,536$ matrix which was used to perform the PCA at a given Gabor filter period (see also Figure 2-1) is reconsidered, and each row of the matrix (corresponding to each cell) is multiplied by the first principal component obtained from the PCA. This yields a scalar corresponding to each cell. A column of 236 scalars is therefore obtained at each Gabor filter period. When all 100 filter periods are considered, a Feature Matrix of scalars with dimensions 236×100 is formed (False color image). The color scale corresponds to the Feature Matrix scalars normalized along each row by dividing the values in each row by the maximum value found for that same row. The data were normalized here for clarity of presentation. However, the classification was done using the raw values of the scalars obtained after the initial multiplication. 25

Figure 2-6 Receiver Operating Curves (ROC) obtained after classifying the Bax/Bak expressing cells (W2) and Bax/Bak double-knockout cells (D3). Using the Feature Matrix generated by the PCA, a supervised linear discriminant classifier was trained to differentiate the W2 from the D3 cells. The cell data were segregated into two groups: 70% of the cells were used for training, and 30% were used to test the classifier. The procedure was repeated 10 times, each time choosing the training and test groups randomly. The results show 10 overlapping ROC curves with an average area-under-the-curve (AUC) of 0.993. The accuracy was taken as $(TP+TN) / (\text{Total number of cells})$. TP: True positives, TN: True negatives..... 26

Figure 2-7 Feature Selection. A feature selection algorithm was implemented to find the Gabor filter periods (columns of the Feature Matrix in Figure 2-5) which are most significant to differentiate between the Bax/Bak expressing cells (W2) and the Bax/Bak double knockout cells (D3). A: The feature selection algorithm sequentially increased the number of Gabor filter periods included in the classification and calculates the misclassification error (MCE) as $(FP+FN) / (\text{Total number of cells})$. FP: False positives, FN: False negatives. The error is significantly decreased after including 20 filters. The feature selection algorithm was then run 10 times after setting the number of features to be used to 20 (inset in Panel A). B: Frequency of filters obtained after running the feature selection algorithm 10 times and specifying the number of filters to be used to 20. 19 filters appeared with a frequency of greater than 3 and were taken as representing the main structural feature sizes (see also Table 2-1) accounting for the differences between the classified W2 and D3 cells..... 28

Figure 2-8 Classification results with selected filters. With the same procedure as in Figure 2-6, the classifier was rerun utilizing only the 19 filters found after feature selection (Refer to Figure 2-7). The new average AUC was 0.956 and the accuracy was 89.8%. 29

Figure 3-1 Optical setup. The OSI technique involves the acquisition of dark-field, filtered images on the charge-coupled device (CCD) camera. Two-dimensional (2D) Gabor filters are displayed on a Liquid Crystal Device (LCD) in the Fourier plane. L₁ and L₂: relay lenses, PBS: polarizing beam splitter, LP= linear polarizer, F1 and F2: conjugate Fourier planes, I₁ and I₂: conjugate imaging planes. 43

Figure 3-2 Flow-chart of the algorithm utilized for image analysis. 45

Figure 3-3 Dark-field (A), Gabor-filtered ($S=2.0$, $\varphi=225^\circ$) (B), phase-congruency (maximum moment) (C) Local Energy (D), and Orientedness (E) images of a

representative cell. Note, edges are enhanced in the phase-congruency (maximum moment) image.	50
Figure 3-4 Four pixel clusters labeled in blue, turquoise, yellow and red. Top panels: pre-treatment, and bottom panels: post-treatment. Each of these clusters contains objects with different scattering profiles and intensities. Note also how the shape of the labeled objects changes with treatment; particularly elongated objects in the turquoise-cluster become smaller and rounder.	52
Figure 3-5 Color-coded centroid values are arranged in a 4x6 polar plot corresponding to 4 orientations and 6 periods for each label shown in Figure 3-4. In both pre- and post-treatment cases, the centroid components of the turquoise and red clusters' demonstrate variation over orientations (ϕ) as well as periods (S), while those of the blue and yellow clusters have low signal with little or no variation. B: The turquoise and red clusters are added together to produce a combined final binary mask.	52
Figure 3-6 Masked Orientedness image of a representative cell. Gradual change in the subcellular scatterers and shape of the dynamic mask can be observed upon injury at t=0.	53
Figure 3-7 Differential interference contrast (DIC) image of a cell undergoing calcium-overloading. Long objects (arrow) observed in the pre-treatment image (left) fragment and become round due to excessive calcium (right). The cell also shrinks which is indicated by trace-marks of the cell membrane (arrow-head). When compared with MitoTracker labeled fluorescent images, the fragmented and rounded long objects in the DIC images correspond to mitochondria (Figure 3-8).....	53
Figure 3-8 MitoTracker labeled fluorescent images show mitochondrial fragmentation and remodeling upon calcium-overloading.	54
Figure 3-9 Classified images generated using the multi-channel Gabor-filtered images (left) and the single unfiltered dark-field image (right).	55
Figure 3-10 Segmented subcellular objects become rounder after calcium overload, as indicated by the aspect-ratio (A) and Orientedness (B). The decrease in the aspect ratio of objects within the fluorescence images (C) suggests that the change in the aspect ratio of mitochondria partially accounts for the decrease in the masked subcellular objects' aspect ratio. The data show mean and standard error for n=6 cells for the first 6 timepoints (treated) and the first 7 timepoints (control). Additional timepoints were tested for one control cell and 4 of the treated cells.	56

Figure 3-11 Changes in the texture-features of the masked orientedness images shown as heat-maps. Each row is a feature while each column is a time-point. Cells were monitored for different time periods, but for at least 180 seconds, after ionomycin treatment (t=0, Treated), or the same saline solution but with no ionomycin (t=0, Control). Texture-features are sensitive to the change in the spatial arrangement of the morphometric parameter Orientedness. The colorscale represents the magnitude of each parameter. 57

Figure 3-12 Average responses of the individual texture features over time. The smoothness of the texture decreases as the Contrast and Dissimilarity increase and IDM (also known as homogeneity) decreases in the treated cells compared with controls. The uniformity of the texture decreases as the Entropy increases whereas the Energy and Max. Probability decrease. Correlation between pixels increases. The data show mean +/- standard error for timepoints at which more than one cell was tested. 58

Figure 3-13 Composite feature calculated from representative features: Autocorrelation, Contrast, Entropy, Energy and IDM. The data show mean +/- standard error for timepoints at which more than one cell was tested. 59

Figure 4-1 Evolution of orientedness in neuronal processes. (top) mCherry transfected mitochondria located in neuronal processes in DIC image (bottom) Orientedness image of the ROI with yellow border. Note the highly oriented edges of the processes compared to the intracellular mitochondria. Colorbar indicates Orientedness values (a.u.). The sample is treated with 120µM glutamate. 71

Figure 4-2 Tracking change in organelle-shape in an un-transfected neuronal processe (yellow ROI). (A) mCherry transfected mitochondria located in neuronal processes in DIC image (B-top) Dark-field images showing time-lapse images of an organelle changing its shape.(B-middle) corresponding S_{max} images indicating difference in size and (B-bottom) histogram showing the distribution of sizes, i.e. S_{max} values. The sample was treated with 120µM glutamate. 75

Figure 4-3 Most frequent S_{max} value in the ROI over time may be used to track the morphological changes in the images object. 76

Figure 4-4 Kymograph showing organelle spatial movement over time (same ROI of Figure 4-2 A). (top) Time-lapse Segmented images; black line indicates the probe for kymograph, (bottom) Kymograph along the black lines on the labeled images over time. Organelle fission at 1.20min can be noticed along with displacement over time. The sample was treated with 120µM glutamate. 77

Figure 4-5 Comparing kymographs generated from label-free Segmented and MitoTracker labeled fluorescent images. (top) time-lapse Segmented image (mid) time-lapse MitoTracker (MT) fluorescent image and dark-field (DF) images (bottom) kymograph obtained from the Segmented images track both labeled and unlabeled mitochondria whereas the fluorescent kymograph tracks organelle as long as it is fluorescing or not bleached. This is a control sample with no glutamate treatment..... 80

Figure 4-6 Signal from broader processes dominate S_{max} image (A) DIC image showing a neuron with axon which is broader (arrow-head) than a thin processes (arrow) (B) mCherry transfected neuron shows location of mitochondria (C) dark-field image (D) S_{max} image showing the S_{max} values in two ROIs. The axon shown in the DIC image is probed by the biggest period and hence colored blue. The mitochondria, shown in red in the fluorescent image, are not visible in the S_{max} image..... 83

Figure 5-1 Basis functions of PCA and NMF. (top panel) principal components (PCs) of PCA and (bottom panel) basis functions of NMF contain different physiological features of a section of a neuronal processes. Note, the basis vectors of NMF (W1 and W2) contain the physiological features of the neuronal processes better compared to the PCs (PC1). Color indicates intensity of the vectors..... 88

Figure 5-2 Brain-on-a-chip device. Image Courtesy: JP Dolle..... 90

Figure 5-3 Neuronal culture in micro-device. (A, B) Phase-contrast images showing neurons in a reservoir and processes stretching through the channels (C) Fluorescent image showing mitochondrial location in the processes (D) Dark-field image showing part of two channels containing processes..... 92

LIST OF TABLES

Table 2-1: Gabor filter periods associated with the 19 filters obtained from the feature selection step.....	29
Table 3-1 Expression for Gabor filters in frequency domain.....	65

CHAPTER 1

1 INTRODUCTION AND REVIEW OF RELATED WORK

1.1 Live-cell Imaging: current gold-standard

Traditionally, organelles in live cells are visualized either by staining with dyes or by expressing organelle-targeted fluorescent proteins. However, such approaches can have adverse effects on organelle function. In particular, fluorescent labels have adverse effects on mitochondrial metabolism¹ and dynamics², which can ultimately hinder reliable drug screening. For example, MitoTracker dyes reduce cell motility in primary neuronal culture as well as alter their morphology². Besides, some dyes are not photo-stable if used in low concentration to avoid quenching effects, whereas fluorophores tend to aggregate and stain other organelles if used in high concentration³. On the other hand, mitochondria targeted fluorescent proteins such as mito-GFP do not affect function or morphology; however, long-duration time-lapse imaging is not possible due to photo-toxicity¹. Moreover, low transfection efficiency hinders High Throughput Screening (HTS) for drug discovery⁴. Hence a label-free imaging technique would be ideal for noninvasive quantification of organelle dynamics over a long period.

1.2 Live-cell Imaging with Optical Methods

There is a wide range of label-free modalities which have been extensively used and popularized for live-cell imaging. However, we should note that each of these approaches has its own merit which makes it appropriate for a specific application. For example, some techniques report the optical properties such as refractive index and absorption, whereas others reveal information regarding metabolic response, stiffness or morphology

of the whole cell and subcellular organelles. Here we present a brief discussion of these label-free imaging techniques as an impetus to cast the advantages of our optical Fourier filtering based scatter imaging in a few specific applications.

1.2.1 Imaging Based on Elastic Scattering

Imaging based on elastic scattering of light has enabled label-free detection and quantification of subcellular structural properties and dynamics pertaining to a biological process without the use of any exogenous marker⁵. Unlike fluorescence imaging, scattering does not involve photon absorption and is several orders of magnitude greater than fluorescence. The magnitude, phase and the angular or wavelength dependence of the scattered far-field can be exploited to provide useful information regarding the scattering object. These attributes of the scattered signal can be obtained either by spectroscopic means or through imaging. While spectroscopy provides overall statistical properties of the whole population of scatterers, light scattering based imaging enables registration of the scattering signal spatially with the scattering sources, thus localizing any change in the scattering profile in a biological sample. Of particular interest to this work is the imaging aspect of light scattering, hence discussion will be limited to the modalities that report scattering data as image. Light scattering has been used to differentiate among human colon cancer cell types with different mutations by measuring the spatial fluctuations in macromolecular density in the cell⁶. The probed fluctuations are reported to be in nanoscale and hence genetic mutations could be identified even though there was no indication of such in the cytological images. Other examples of imaging modalities based on light scattering include Optical Coherence Tomography

(OCT), Quantitative Phase Imaging (QPI) and Second Harmonic generation (SHG). which are discussed below.

1.2.1.1 Optical Coherence Tomography (OCT)

OCT uses back-scattered light to perform cross-sectional and 3D imaging of the internal microstructure in tissue samples. The heart of the technique is a Michelson interferometer that combines the back-scattered light from the sample with the reflection from a reference mirror. Based on the interference pattern and the low coherence length of the light source, the longitudinal location of the back-scattering can be obtained from this interferometric signal. Thus a depth-profile of the sample structure can be constructed⁷. More recently, a high-resolution version of OCT called micro OCT (μ OCT) has been developed⁸ that is capable of resolving 1-2 μ m, enabling visualization of individual cells and subcellular features *in vivo*. Although OCT is widely used to generate histology-like images of tissue structure, studies have also been conducted on thinner samples such as cell monolayer⁹. There, real-time detection of cell death is performed using the backscattering coefficient (i.e. amount of light scattered back) integrated over the numerical aperture which reported a significant change in scattering upon the induction of apoptosis. This change is shown to be related to the changes in mitochondria almost directly after the onset of apoptosis, indicating the efficacy of OCT for detection of scattering linked to the alterations in mitochondrial morphology. In addition, OCT has also been applied to assess cell activities in three-dimensional cell-based tissue models providing insights of the 3D organization of cells and their chemotaxis migration, proliferation, de-adhesion, and cell-material interactions¹⁰.

1.2.1.2 Quantitative Phase Imaging (QPI)

QPI measures the phase shift in the incident light produced by a specimen, providing useful information about local thickness and refractive index of the imaged structure¹¹. A large number of experimental setups for QPI have been developed in a wide range of applications such as cell imaging for morphology, monitoring cell-growth¹², mapping dry mass¹³, membrane fluctuations¹⁴, blood screening¹¹ and cancer diagnosis¹⁵. Specifically, QPI based Spatial Light Interference Microscopy (SLIM) can be used to report optical path-length fluctuations along neurites, revealing inhomogeneity associated with synaptic structures in neurons¹⁶. In addition, QPI techniques can be augmented with mathematical operators to produce enhanced phase images. One such example is Laplace Phase Microscopy (LPM) where the final image is computed via Laplace operator on the images collected by SLIM. This technique has been applied to study organelle transport in the processes of the live hippocampal neurons¹⁷.

1.2.2 Second Harmonic generation (SHG)

SHG takes advantage of the non-linear polarization in the specimen induced by an intense incident light. In effect, this process produces a coherent wave at exactly twice the incident frequency, i.e. harmonic¹⁸. However, only the biological materials that are highly ordered and birefringent such as type I and II collagen¹⁹ and myosin within actomyosin complexes²⁰ can generate second harmonics. SHG has been applied to measure the membrane potential dynamics in cultured mouse hippocampal neurons²¹ and to characterize microtubules in brain slices from Alzheimer's disease transgenic mouse models²².

1.2.3 Two Photon Excitation Fluorescence (TPEF)

TPEF and SHG are somewhat similar techniques, however, while the second harmonic is generated by the scattering of photons, in TPEF the photons are absorbed by the target to produce a single photon at a higher energy (Perry 2012). For label-free TPEF, endogenous fluorescent molecules such as mitochondrial matrix proteins reduced nicotinamide adenine dinucleotide (phosphate) (NAD(P)H), and flavin adenine dinucleotide (FAD)^{23, 24} are excited and monitored that are indicative of the underlying biochemical processes and metabolism. Using these intrinsic fluorophores, differential metabolic changes in different brain cell types in response to neurotoxins is reported by TPEF²⁵. In addition, multiple sources of this intrinsic emission is identified and characterized in the brain slices of Alzheimer's disease mouse models²².

1.2.4 Brillouin Microscopy

On the other hand, Brillouin microscopy can be used to measure the biomechanical properties of cells. As the name suggests, this technique takes the advantage of the Brillouin light scattering. It measures the frequency shift in the incident light upon interaction with acoustic phonons from which the longitudinal modulus can be determined²⁶. This technique is used to assess mechanical properties such as the modulus of cytoskeletal components, network cross-linking of cellular microenvironment in unstained cells. Recently, this technique has been used to assess the viscoelastic properties of amyloid plaques in β -amyloid overexpressing transgenic mouse brain, providing a novel contrast mechanism and tool for the diagnosis of Alzheimer's disease²⁷.

1.2.5 Super-resolution Microscopy

In attempting to overcome the diffraction barrier of classical optical microscopy, scientists have developed super-resolution microscopy which can resolve features below the wavelength of light²⁸. Through elegant optical tricks, this emerging class of imaging techniques has enabled visualization of subcellular structures and processes with unprecedented details. However, these techniques were originally designed for fluorescent samples and hence predominantly limited to resolve features tagged with exogenous markers. Unfortunately, fluorophore based super-resolution techniques may still suffer from photo-bleaching, photo-toxicity. In addition, some setups have specific requirements for sample preparation and high acquisition time²⁸. In other words, fluorescence based fast, high contrast super-resolution technique still does not exist²⁹. To circumvent these issues, several label-free super-resolutions techniques have been proposed²⁹⁻³². Some of these techniques fall in the category of Structured Illumination Microscopy (SIM), a variation of super-resolution microscopy where the intensity of the illumination beam is modulated spatially, and thus the object spectra is aliased and shifted beyond the cut-off imposed by the objective's aperture. Upon repetition over different spatial directions, a frequency spectrum twice as big of the original aperture can be obtained, thus enhancing the resolution by two-fold²⁸. It has been shown numerically that four- and six-fold improvement in the resolution can be achieved from nonlinear SIM where the phase of the illumination is modulated instead of intensity and subsequent second and third harmonics are exploited³⁰. Another strategy is to use oblique illumination using a rotating coherent source in totally internal reflected (TIR) and dark-field setup²⁹. Oblique illumination generates phase delay in the fields emitted by two

adjacent scatters, resulting in destructive interference which helps to enhance the contrast of the specimen. To the best of our knowledge, however, none of these label-free techniques have been applied to image neurons or mitochondria.

1.2.6 Fourier Ptychography

Fourier ptychography microscopy (FPM) is a computational imaging approach which can provide high-resolution images of a sample by bypassing the physical limit of the imaging system. This is achieved by combining phase retrieval and aperture synthesis technique³⁶. The image acquisition involves illuminating the sample from different angles with a LED matrix and collecting low-resolution intensity images through a low NA objective. By the computational techniques mentioned above, the raw images are processed to generate a complex image which contains both the intensity and phase. FPM has been used to study the phenotypic behavior of microglial cells in primary neuronal co-cultures through the addition of cyclosporine A³⁷.

1.3 Previous Work

As mentioned before, light scattering by subcellular organelles and interfaces such as membranes can be utilized for quantitative measurement of cellular and tissue states⁵. Structural information of the subcellular organelles can be inferred from scattering by analyzing the diffraction pattern at a conjugate Fourier plane of the imaging system. Via implementation of Gabor filters on the Fourier plane, we can selectively allow only certain angles of scattering to pass. These scatter angles are directly related to the spatial frequencies of the scattering source. So in effect, the Gabor filters can probe objects of certain size/shape and orientation. The filters are characterized by 3 parameters: period, orientation and standard deviation. The standard deviation is scaled with the period of the

filter. Filter response is the maximum when width of the scattering source is approximately half of the filter period and/or if the source is oriented at perpendicular to the filter's orientation. Due to the linear relationship between filter period and the width of the scattering source, resultant images inherently encode specimen's structural size information in terms of filter periods^{33, 34}. Likewise, an object's orientation can also be encoded in the filtered images. Based on this property, a morphometric parameter called Orientedness was proposed to indirectly probe the geometric aspect ratio of subcellular organelles. It was demonstrated that Orientedness is sensitive to the morphological changes related to mitochondrial fission during apoptosis in Bovine Aortic Endothelial Cells (BAEC)³⁵.

A common theme of this thesis is the assessment of mitochondrial morphology under normal and dysregulated conditions. In chapter 2, we demonstrate that our Gabor-filtering based imaging system is able to detect morphological alterations in mitochondria due to genetic mutation in apoptosis-resistant cells. The merit of the proposed technique is that the detection does not require an individual mitochondrion to be optically resolved. On the contrary, in chapter 3, we demonstrate that the technique can also track changes in optically well-resolved mitochondrial length and shape in endothelial cells upon calcium-injury. In chapter 4, we applied the imaging technique to track organelle morphology and transport in neuronal processes. Using fluorescence images for validation, we track mitochondrial movement and dynamics in the processes. Finally, in chapter 5 we propose future directions for the techniques developed in this thesis.

References

1. Dixit R, Cyr R. Cell damage and reactive oxygen species production induced by fluorescence microscopy: effect on mitosis and guidelines for non-invasive fluorescence microscopy. *The Plant Journal*. 2003;36(2):280-90.
2. Buckman JF, Hernández H, Kress GJ, Votyakova TV, Pal S, Reynolds JJ. MitoTracker labeling in primary neuronal and astrocytic cultures: influence of mitochondrial membrane potential and oxidants. *Journal of neuroscience methods*. 2001;104(2):165-76.
3. Zhao Q, Huang, Chunhui, Li, Fuyou. Phosphorescent heavy-metal complexes for bioimaging. *Chem Soc Rev*. 2011;40(5):17.
4. Zhang ZG, Ni; Li, Ting; Mais, Dale E.; Wang, Mingwei. Quality control of cell-based high-throughput drug screening. *Acta Pharmaceutica Sinica B*. 2012;2(5):10.
5. Boustany NN, Boppart SA, Backman V. Microscopic imaging and spectroscopy with scattered light. *Annual review of biomedical engineering*. 2010;12:285-314.
6. Subramanian H, Pradhan P, Liu Y, Capoglu IR, Li X, Rogers JD, et al. Optical methodology for detecting histologically unapparent nanoscale consequences of genetic alterations in biological cells. *Proceedings of the National Academy of Sciences*. 2008;105(51):20118-23.
7. Huang D, Swanson EA, Lin CP, Schuman JS, Stinson WG, Chang W, et al. Optical coherence tomography. *Science*. 1991;254(5035):1178-81.
8. Liu L, Gardecki JA, Nadkarni SK, Toussaint JD, Yagi Y, Bouma BE, et al. Imaging the subcellular structure of human coronary atherosclerosis using micro-optical coherence tomography. *Nature medicine*. 2011;17(8):1010.
9. de Bruin DM, Broekgaarden M, van Gemert MJ, Heger M, de la Rosette JJ, Van Leeuwen TG, et al. Assessment of apoptosis induced changes in scattering using optical coherence tomography. *Journal of biophotonics*. 2016;9(9):913-23.
10. Tan W, Oldenburg AL, Norman JJ, Desai TA, Boppart SA. Optical coherence tomography of cell dynamics in three-dimensional tissue models. *Optics Express*. 2006;14(16):7159-71.
11. Mir M, Bhaduri B, Wang R, Zhu R, Popescu G. Quantitative phase imaging. *Progress in Optics*. 2012;57:133-217.
12. Rappaz B, Cano E, Colomb T, Kuhn J, Depeursinge CD, Simanis V, et al. Noninvasive characterization of the fission yeast cell cycle by monitoring dry mass with digital holographic microscopy. *Journal of biomedical optics*. 2009;14(3):034049.
13. Zicha D, Genot E, Dunn GA, Kramer IM. TGFbeta1 induces a cell-cycle-dependent increase in motility of epithelial cells. *Journal of Cell Science*. 1999;112(4):447-54.
14. Popescu G, Ikeda T, Goda K, Best-Popescu CA, Laposata M, Manley S, et al. Optical measurement of cell membrane tension. *Physical review letters*. 2006;97(21):218101.
15. Wang Z, Popescu G, Tangella KV, Balla A. Tissue refractive index as marker of disease. *Journal of biomedical optics*. 2011;16(11):116017.
16. Wang Z, Marks DL, Carney PS, Millet LJ, Gillette MU, Mihi A, et al. Spatial light interference tomography (SLIT). *Optics express*. 2011;19(21):19907-18.

17. Wang Z, Ding H, Bashir R, Popescu G, Millet L, Gillette M, et al. Label-free intracellular transport measured by spatial light interference microscopy. *Journal of Biomedical Optics*. 2011;16(2):026019.
18. Mohler W, Millard AC, Campagnola PJ. Second harmonic generation imaging of endogenous structural proteins. *Methods*. 2003;29(1):97-109.
19. Campagnola P. Second harmonic generation imaging microscopy: applications to diseases diagnostics. ACS Publications; 2011.
20. Campagnola PJ, Millard AC, Terasaki M, Hoppe PE, Malone CJ, Mohler WA. Three-dimensional high-resolution second-harmonic generation imaging of endogenous structural proteins in biological tissues. *Biophysical journal*. 2002;82(1):493-508.
21. Nuriya M, Yasui M. Membrane potential dynamics of axons in cultured hippocampal neurons probed by second-harmonic-generation imaging. *Journal of Biomedical Optics*. 2010;15(2):020503.
22. Kwan AC, Duff K, Gouras GK, Webb WW. Optical visualization of Alzheimer's pathology via multiphoton-excited intrinsic fluorescence and second harmonic generation. *Optics Express*. 2009;17(5):3679-89.
23. Zipfel WR, Williams RM, Webb WW. Nonlinear magic: multiphoton microscopy in the biosciences. *Nature biotechnology*. 2003;21(11):1369.
24. Skala MC, Ricking KM, Gendron-Fitzpatrick A, Eickhoff J, Eliceiri KW, White JG, et al. In vivo multiphoton microscopy of NADH and FAD redox states, fluorescence lifetimes, and cellular morphology in precancerous epithelia. *Proceedings of the National Academy of Sciences*. 2007;104(49):19494-9.
25. Stuntz E, Gong Y, Sood D, Liaudanskaya V, Pouli D, Quinn KP, et al. Endogenous two-photon excited fluorescence imaging characterizes neuron and astrocyte metabolic responses to manganese toxicity. *Scientific reports*. 2017;7(1):1041.
26. Scarcelli G, Polacheck WJ, Nia HT, Patel K, Grodzinsky AJ, Kamm RD, et al. Noncontact three-dimensional mapping of intracellular hydromechanical properties by Brillouin microscopy. *Nature methods*. 2015;12(12):1132.
27. Mattana S, Caponi S, Tamagnini F, Fioretto D, Palombo F. Viscoelasticity of amyloid plaques in transgenic mouse brain studied by Brillouin microspectroscopy and correlative Raman analysis. *Journal of innovative optical health sciences*. 2017;10(06):1742001.
28. Vangindertael J, Camacho R, Sempels W, Mizuno H, Dedecker P, Janssen K. An introduction to optical super-resolution microscopy for the adventurous biologist. *Methods and applications in fluorescence*. 2018;6(2):022003.
29. Jünger F, Olshausen Pv, Rohrbach A. Fast, label-free super-resolution live-cell imaging using rotating coherent scattering (ROCS) microscopy. *Scientific reports*. 2016;6:30393.
30. Huttunen MJ, Abbas A, Upham J, Boyd RW. Label-free super-resolution with coherent nonlinear structured-illumination microscopy. *Journal of Optics*. 2017;19(8):085504.
31. Littleton B, Lai K, Longstaff D, Sarafis V, Munroe P, Heckenberg N, et al. Coherent super-resolution microscopy via laterally structured illumination. *Micron*. 2007;38(2):150-7.
32. Mudassar AA, Hussain A. Super-resolution of active spatial frequency heterodyning using holographic approach. *Applied optics*. 2010;49(17):3434-41.

33. Sierra H, Zheng J-Y, Rabin B, Boustany NN. Measurement of object structure from size-encoded images generated by optically-implemented Gabor filters. *Optics express*. 2012;20(27):28698-706.
34. Pasternack RM, Zheng J-Y, Boustany NN, editors. Quantifying mitochondrial dynamics in apoptotic cells with optical Gabor-like filtering. *Biomedical Optics*; 2010: Optical Society of America.
35. Pasternack RM, Zheng JY, Boustany NN. Detection of mitochondrial fission with orientation-dependent optical Fourier filters. *Cytometry Part A*. 2011;79(2):137-48.
36. Zheng, G., Breakthroughs in Photonics 2013: Fourier Ptychographic Imaging, *IEEE Photonics Journal*, vol. 6, no. 2, pp. 1-7, April 2014, Art no. 0701207.
37. Suman, R., Smith, G., Hazel, K. E., Kasprowicz, R., Coles, M., O'Toole, P., & Chawla, S. (2016). Label-free imaging to study phenotypic behavioural traits of cells in complex co-cultures. *Scientific reports*, 6, 22032.

CHAPTER 2

2 LABEL-FREE CLASSIFICATION OF BAX/BAK EXPRESSING VS. DOUBLE-KNOCKOUT CELLS

This chapter includes work published in Naser, Mohammad, et al. "Label-Free Classification of Bax/Bak Expressing vs. Double-Knockout Cells." *Annals of biomedical engineering* 44.11 (2016): 3398-3407, used by permission from Springer Nature under license 4427730140299.

Abstract

We combine optical scatter imaging with principal component analysis (PCA) to classify apoptosis-competent Bax/Bak-expressing, and apoptosis resistant Bax/Bak-null immortalized baby mouse kidney (iBMK) cells. We apply PCA to 100 stacks each containing 236 dark-field cell images filtered with an optically implemented Gabor filter with period between $0.3\mu\text{m}$ and $2.9\mu\text{m}$. Each stack yields an "eigencell" image corresponding to the first principal component obtained at one of the 100 Gabor filter periods used. At each filter period, each cell image is multiplied by (projected onto) the eigencell image. A Feature Matrix consisting of 236×100 scalar values is thus constructed with significantly reduced dimension compared to the initial dataset. Utilizing this Feature Matrix, we implement a supervised linear discriminant analysis and classify successfully the Bax/Bak-expressing and Bax/Bak-null cells with 94.7% accuracy and an area under the curve (AUC) of 0.993. Applying a feature selection algorithm further reveals that the Gabor filter periods resulting this classification accuracy correspond to both large (likely nuclear) features as well as small sized features (likely organelles

present in the cytoplasm). Our results suggest that cells with a genetic defect in their apoptosis pathway can be differentiated from their normal counterparts by label-free multi-parametric optical scatter data.

2.1 Introduction

Recent reports have suggested that light scattering (LS) spectroscopy of cells and tissues can differentiate between normal and diseased samples¹. The clinical value of these LS approaches for minimally-invasive cancer diagnosis or cancer risk-assessment has been demonstrated by several investigators²⁻⁷ with potential high impact on patient outcomes.

Cancer is a disease involving sequential mutations affecting critical molecular pathways regulating cell growth and the maintenance of tissue homeostasis^{8, 9}. As demonstrated in colorectal cancer¹⁰, mutations leading to cellular transformation correlate with tumor formation as well as the histopathological progression from hyper-proliferative epithelium to adenoma to carcinoma as more oncogenic mutations are acquired. Based on this and similar histopathological progression observed in other epithelial tumors, the morphological changes involving dysplasia and neoplasia have become an important target of LS technologies aimed at epithelial cancer diagnosis¹¹⁻¹³. Current LS technologies which are used for diagnosis of cancer have shown that light scattering can detect subtle and important morphological changes with high sensitivity and specificity in differentiating normal from diseased tissue¹³⁻¹⁶. More recently, “histopathologically unapparent” structural changes in cancer cells were detected by light scattering¹⁶⁻¹⁸. These results are remarkable in that they demonstrate that LS can detect the early transformation of cells and has the potential for early and minimally-invasive diagnosis.

Transformed neoplastic cells such as those investigated previously¹⁸ possess several accumulated mutations which may give rise to alterations in light scattering properties. In this paper, we investigate if a single mutation could lead to optical scatter changes. For this, we use an immortalized baby mouse kidney (iBMK) cell model¹⁹ and measure the angular scattering properties of apoptosis-competent Bax/Bak-expressing iBMK cells vs. Bax/Bak-double knockout apoptosis-resistant and tumor-forming cells. Except for the Bax/Bak mutation, the cells are isogenic, and indistinguishable by high magnification microscopic observation with phase contrast or differential interference contrast. We choose to investigate Bax/Bak mutation because the vast majority, if not all, of human tumors exhibit genetic alterations in the pathways controlling growth arrest and apoptosis through inhibition of p53 and Bax/Bak-mediated apoptosis²⁰. Bax/Bak-mediated apoptosis is a well-known and ubiquitous tumor suppression mechanism which prevents cell survival and genomic instability, two fundamental properties required for tumor growth. As such, detecting Bax/Bak knockout cells with label-free light scattering could provide a basis for ultimately detecting cells which have acquired the apoptosis resistance “hallmark”⁸.

For our study, we utilize an Optical Scatter Imaging (OSI) technique which is sensitive to changes in organelle size and shape²¹⁻²³. The technique relies on optically-implemented Gabor filters with varying periods and/or orientations to probe the scatter plane and collect multiple stacks of filtered dark-field images with different angular light scattering contributions. Here we combine this technique with principal component analysis (PCA) to reduce the dimension of the stacks of raw images into a single feature

matrix that can be used to classify the two variants of iBMK cells (Bax/Bak expressing and double knockout).

2.2 Materials and Methods

2.2.1 Cell preparation

iBMK cells expressing Bax and Bak (W2), and Bax/Bak double-knockout iBMK cells (D3) were generously provided by the laboratory of Dr. E. White at the Rutgers Cancer Institute of New Jersey. iBMK cells were maintained in high glucose Dulbecco's Modified Eagle's Medium (DMEM) supplemented with 10% fetal bovine serum (FBS) (V:V), 100-units/ml penicillin, and 100- μ g/ml streptomycin in a humidified incubator at 38°C and 5% CO₂. The cells' response to an apoptosis inducer was previously tested and demonstrated that the Bax/Bak expressing W2 cells are apoptosis-competent while the Bax/Bak-null D3 cells are apoptosis-resistant^{19,24}.

For microscopy, the cells were cultured on uncoated glass coverslips in the DMEM medium described above. During imaging, the coverslips with attached live cells were mounted on a steel plate. The DMEM was replaced with Leibovitz L15 medium (Invitrogen, Carlsbad, California) to maintain a physiological pH in a non-CO₂-equilibrated environment.

2.2.2 Optical Scatter Imaging (OSI)

The imaging setup was described previously²³. Here, laser light ($\lambda_0=532\text{nm}$) was passed through a spinning diffuser and coupled to the condenser port of an inverted microscope via a multimode optical fiber (Thorlabs) to illuminate the sample in central Kohler illumination. Light scattered by the sample was filtered by sequentially displaying a bank

of Gabor filters implemented on a reflective liquid crystal device (LCD, Holoeye Photonics, LC-R- 2500) placed in a conjugate Fourier plane. LCD pixels corresponding to the zeroth order of diffraction were always turned off. The sample was imaged with a 63X oil-immersion objective with numerical aperture (NA) = 1.4. The filtered dark-field images were captured sequentially on the CCD (512 pixels x 512 pixels, Roper Scientific, Cascade 512B) with a magnification of $0.23\mu\text{m}/\text{CCD pixel}$. Similar to Reference 26, a set of 100 Gabor filters were used with filter periods varying between $S = 0.33\mu\text{m}$ and $2.93\mu\text{m}$ at each of two filter orientations, $\phi = 0^\circ$ and 90° . Differential interference contrast (DIC) images of the cells were also collected in each experiment. Background images of culture medium without any cells were collected for every filter. All images were acquired using a custom made Java program that synchronized the LCD display with image acquisition and microscope settings.

2.2.3 Image pre-processing

The filtered dark-field images were processed in Matlab (The MathWorks, Natick, Massachusetts). Each cell was first segmented manually using the unfiltered dark-field image. The segmented cells in the dark-field images were compared side-by-side with their corresponding DIC images for validation at the cell boundaries. Since two separate cameras were used for dark-field and DIC, the two fields of views did not overlap exactly. Some cells which were clearly delineated in dark-field but not included within the DIC field of view were also segmented for further analysis. Segmentation from 10 separate experiments resulted in a total of 236 cell segments of which 135 were D3 and 101 were W2 cells. Seven pairs of cells were fused and were each treated as one large cell. When iBMK cells are in culture, some of them fuse and lose the cell membrane

boundary between them. As such one would see a large cell with two nuclei. In this case, rather than segmenting them individually by drawing an arbitrary cell boundary between them, we used them as one unit. The individual cell segments were zero-padded to produce individual images with 256 x 256 pixels. Before further analysis, each image was thresholded by subtracting the corresponding background image. In addition, pixel values obtained at Gabor filter orientations of 0° and 90° were averaged, such that each cell was eventually associated with 100 filtered images, each consisting of the average between the 0° and 90° images collected at a given Gabor filter period. Each of these background-subtracted and averaged cell images was “stretched” by normalizing its histogram to the maximum image value.

2.2.4 Principal Component Analysis (PCA)

The steps of the PCA are shown in Figure 2-1. For each Gabor filter period, each two-dimensional filtered image of a cell was reshaped into a one-dimensional $1 \times 65,536$, vector. When all 236 cell vectors are considered, a matrix M with dimensions $236 \times 65,526$ results where each row-vector represents a cell. We termed the first dimension of M the cell-dimension (236) and the second pixel-dimension (65,536). We applied PCA over the pixel-dimension of the data matrix M at each Gabor filter period. PCA was implemented with a built-in Matlab routine. Since the Principal Components (PCs) are the eigenvectors of the covariance matrix of the data, the resulting matrix should be square in shape. Hence, applying PCA over the pixel-dimension resulted in PC vectors with 65,536 elements. However, the PC vectors with zero variance are discarded which resulted in a $65,536 \times 235$ matrix. This process was repeated for each of the 100 Gabor filter periods used. Only the first PC, which on average accounted for 9.9% of the

variance, was considered in each case. Since the PCA was performed over the pixel dimension after reshaping the original images into $1 \times 65,536$ vectors, this first PC could be reshaped back into an image for visualization (Figure 2-1). As shown in Figure 2-1, for a given Gabor filter period, this reshaped image PC contains all the significant contributions from all the cells to the filtered images collected at that particular Gabor filter period. We refer to these PC images as “eigencell images” and 100 such images were produced corresponding to each of the Gabor filter periods used in the experiment. Following the PCA, each initial cell vector was reconsidered and multiplied by the first PC vector obtained for each filter period resulting in a single scalar corresponding to each cell’s contribution to the eigencell image. When all 100 filter periods were considered, this process yielded 100 feature values for each of the 236 cells (See Feature Matrix in section 2.3.2.2 in Results).

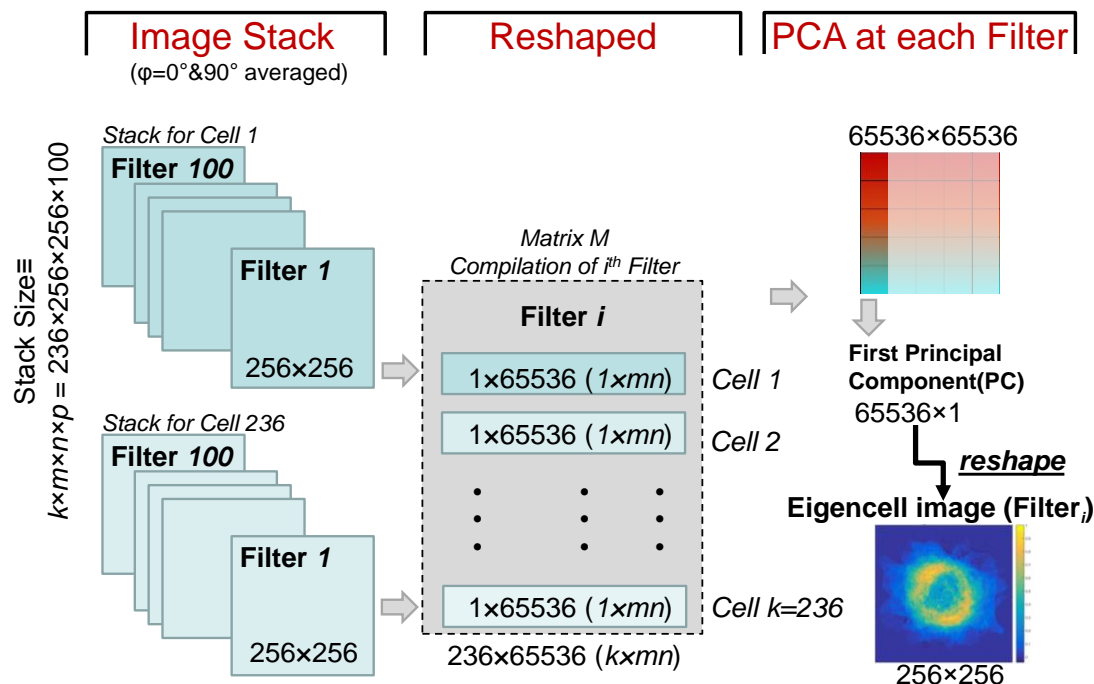


Figure 2-1 Principal component analysis (PCA) of the dark-field image stack at each Gabor filter period. For each Gabor filter period, each cell image is reshaped into a $1 \times 65,536$ vector yielding a $236 \times 65,536$ matrix in which each row represents a cell vector. PCA applied along the pixel dimension yields principal component vectors which are $65,536 \times 1$. Each principal component may be reshaped into an image matrix representing an “eigencell” for the data set at the Gabor filter period analyzed (Filter_i). Only the first principal component was kept, resulting in a total of 100 eigencell images corresponding to each Gabor filter period.

2.2.5 Linear Discriminant Analysis Classifier

To classify the Bax/Bak null (D3) and Bax/Bak expressing (W2) cells, a supervised learning technique implemented by linear discriminant analysis (LDA) was used. LDA finds the linear combination of the variables (i.e. a cell’s contribution to 100 filters in the Feature Matrix) that best defines the two class-labels, “D3” and “W2”, provided during

training. This linear combination of variables generates a hyperplane that works as a decision boundary between the two cell classes. This discriminatory model is then used to classify the unseen test-data. The LDA model was first trained with 70% (D3: 94 and W2: 72 cells) of the data and tested with the rest. The classification step was repeated 10 times, each time picking at random a new training and test set.

2.2.6 Feature Selection Algorithm

To identify the most influential subset of Gabor filter periods that represent the structural differences between D3 and W2 cells, a feature-selection step was performed. The search was implemented in a wrapper fashion where filter subsets (columns in the Feature Matrix) were considered and evaluated. The subsets were created by sequentially adding filters based upon a criterion set by a classifier model. We used the same LDA algorithm described in section 2.2.5 above for the model here. LDA evaluates the performance of each subset in terms of misclassification error and decides whether to keep or discard the filter from the current subset. We used the forward sequential approach for feature selection. For each new filter inclusion, a 10-fold cross-validation was performed to the training set and the misclassification error (MCE) is obtained.

2.3 Results

2.3.1 Representative DIC and dark field images

Representative differential interference contrast (DIC) and dark-field images of Bax/Bak expressing (W2) and Bax/Bak-null (D3) cells are shown in Figure 2-2, Figure 2-3. These images suggest that the two cell variants, which have profound differences in their apoptosis function, are indistinguishable by conventional microscopic observations. While the cells appear qualitatively indistinguishable in Figure 2-2 and Figure 2-3,

further quantitative analysis and classification of the of the optical scatter data by PCA (Section 2.3.2.2) will prove that in fact they can be distinguished. Representative filtered images collected at specific Gabor filter periods and orientation (Bottom panels in Figure 2-2 and Figure 2-3) suggest that filters with high period values (low spatial frequencies) are sensitive to relatively large subcellular features, such as the nucleoli. Gabor filters with low period values (high spatial frequencies) are relatively sensitive to organelles in the cytoplasm.

2.3.2 Feature extraction and detection of genetic mutation

2.3.2.1 Eigencell images

The PC vectors resulting from the PCA at each Gabor filter (Figure 2-1) can be reshaped into eigencell images (Figure 2-4), which represent the contributions of all the cells to the spatial signal distribution at a given Gabor filter period. Eigencell images mirror the filtered dark-field images shown in Figure 2-2, Figure 2-3 to the extent that larger subnuclear particles are prominent at low filter periods while smaller particles in the cytoplasm are prominent at high filter periods. These results suggest that each eigencell image reports on the variance in the spatial distributions of subcellular features with sizes on the order of a given Gabor filter period.

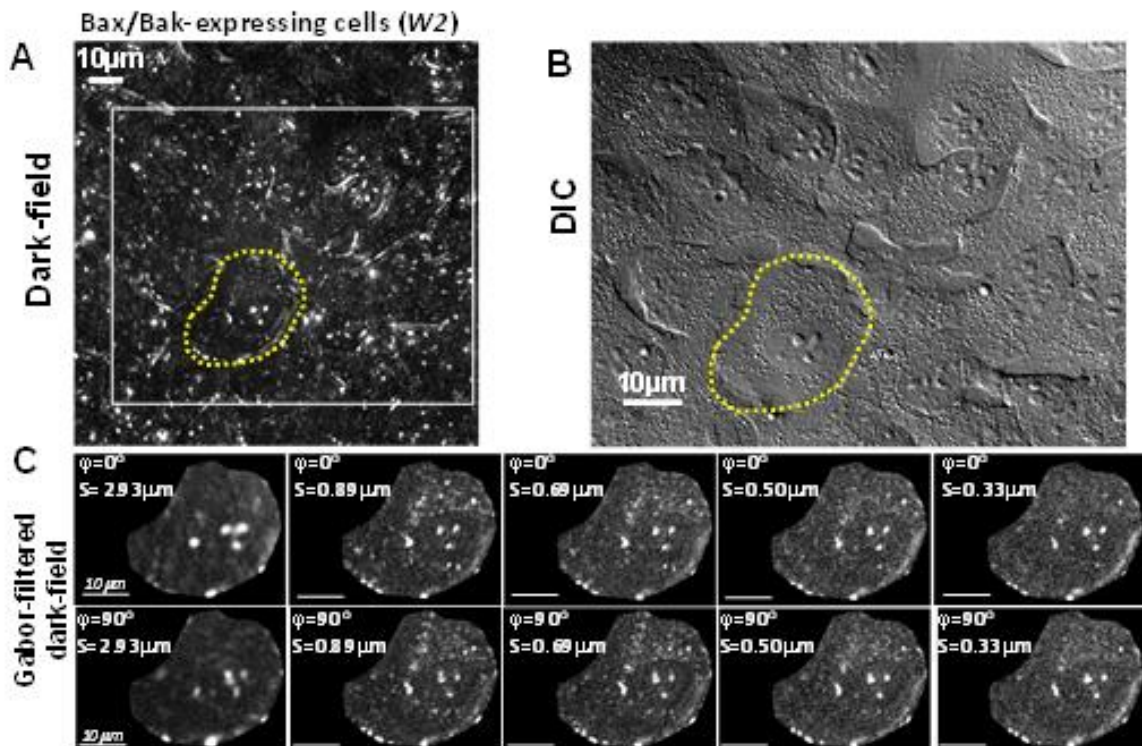


Figure 2-2 Representative images of a Bax/Bak expressing (W2) cell A: Dark-field image showing the full field of view. The white rectangle indicates the region of the field that was also imaged by differential interference contrast (DIC) (B). C: Filtered images of the cell outlined by the yellow dotted line in Panels A and B are shown for several Gabor filters with varying periods, S , and orientation, ϕ , of either 0° or 90° .

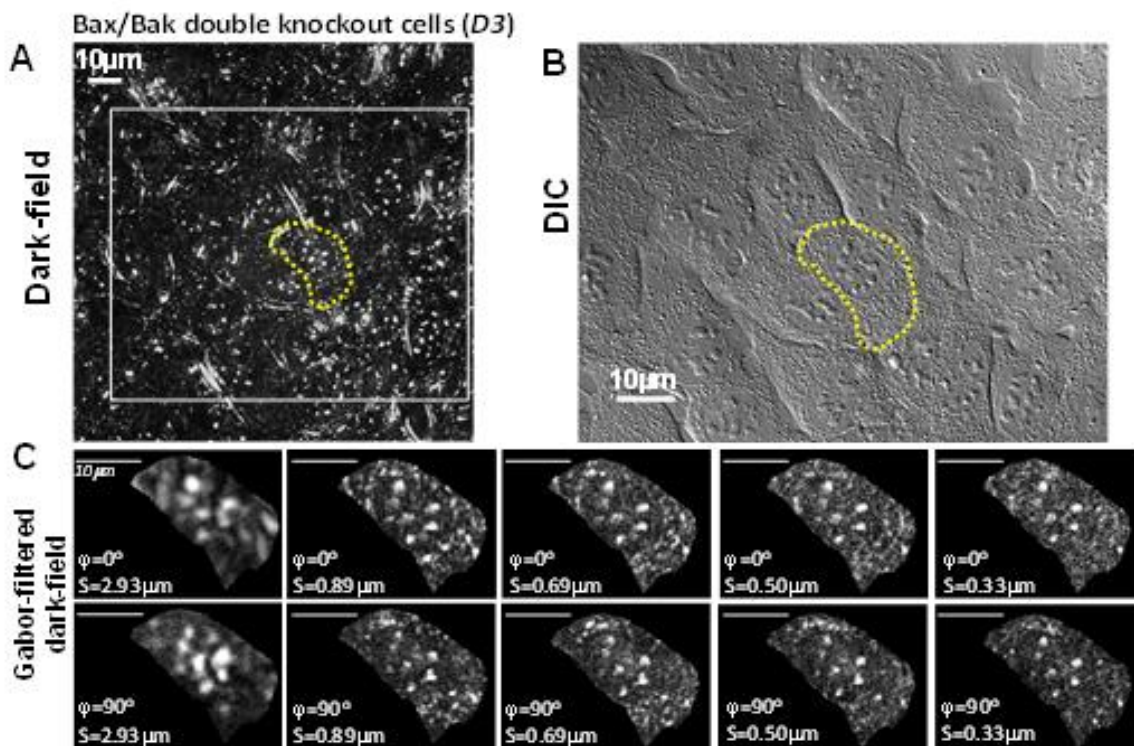


Figure 2-3 Representative images of a Bax/Bak double knockout (D3) cell. A: Dark-field image showing the full field of view. The white rectangle indicates the region of the field was also imaged by differential interference contrast (DIC) (B). C: Filtered images of the cell outlined by the yellow dotted line in Panels A and B are shown for several Gabor filters with varying periods, S , and orientation, φ , of either 0° or 90° .

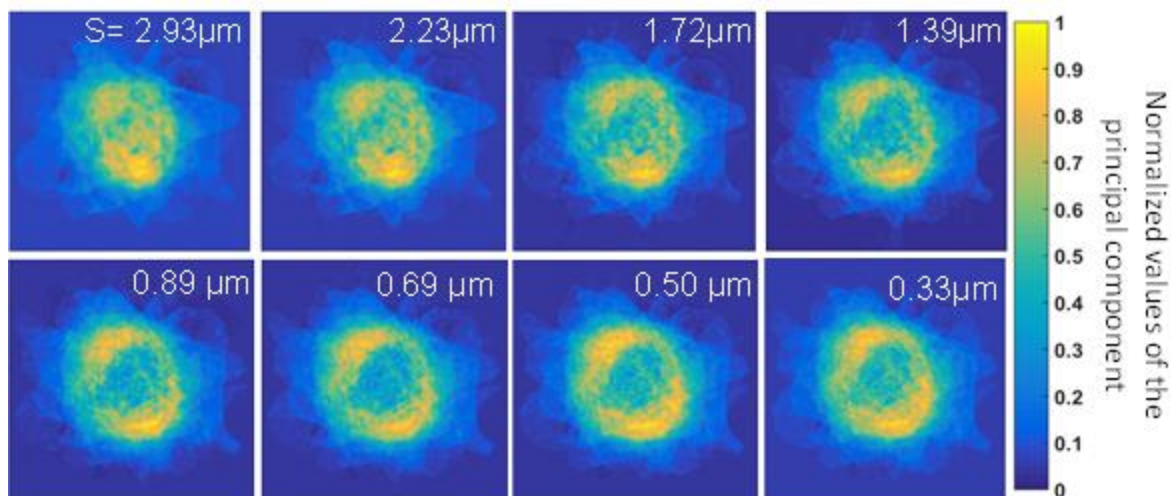


Figure 2-4 Representative eigencell images obtained at 8 different Gabor filter periods. Images taken with Gabor filter orientations at 0° and 90° degrees were averaged together at each Gabor filter period before performing the PCA. The color scale corresponds to the normalized values of the PC vectors from which the eigencell images were formed.

2.3.2.2 Feature calculation from PCA and classification of *Bax/Bak* expressing and *Bax/Bak* double knockout cells

For each Gabor filter period, feature calculation was performed by multiplying each cell image (reshaped as $1 \times 65,536$ vector) with the first $1 \times 65,536$ PC (reshaped eigencell image) found by the PCA described in Figure 2-1. This multiplication results in one scalar, defined as a Feature, for each cell at each filter period. Each Feature represents the projection of a cell onto the PC obtained at a given period, and corresponds to the total contribution of that given cell to the PC at that filter period. When all cells and filters are considered, a Feature Matrix with 236×100 Features is created (Figure 2-5). The Feature Matrix achieves a reduction from the initial dataset dimension of $236 \times 256 \times 256 \times 100$ (after averaging at each Gabor filter period the images collected at 0° and 90°

orientation) to 236×100 . This dimensionally reduced data set may now be used for classification of the Bax/Bak expressing (W2) and Bax/Bak-null (D3) cell populations. We utilized the Feature Matrix to apply a supervised classification approach to differentiate between Bax/Bak null (D3) and Bax/Bak expressing (W2) cells. We applied a linear discriminant analysis (LDA) and classification algorithm and repeated the classification 10 times (Figure 2-6). The results show an average accuracy of 94.7%, and an average area-under-the-curve (ROC) of 0.99.

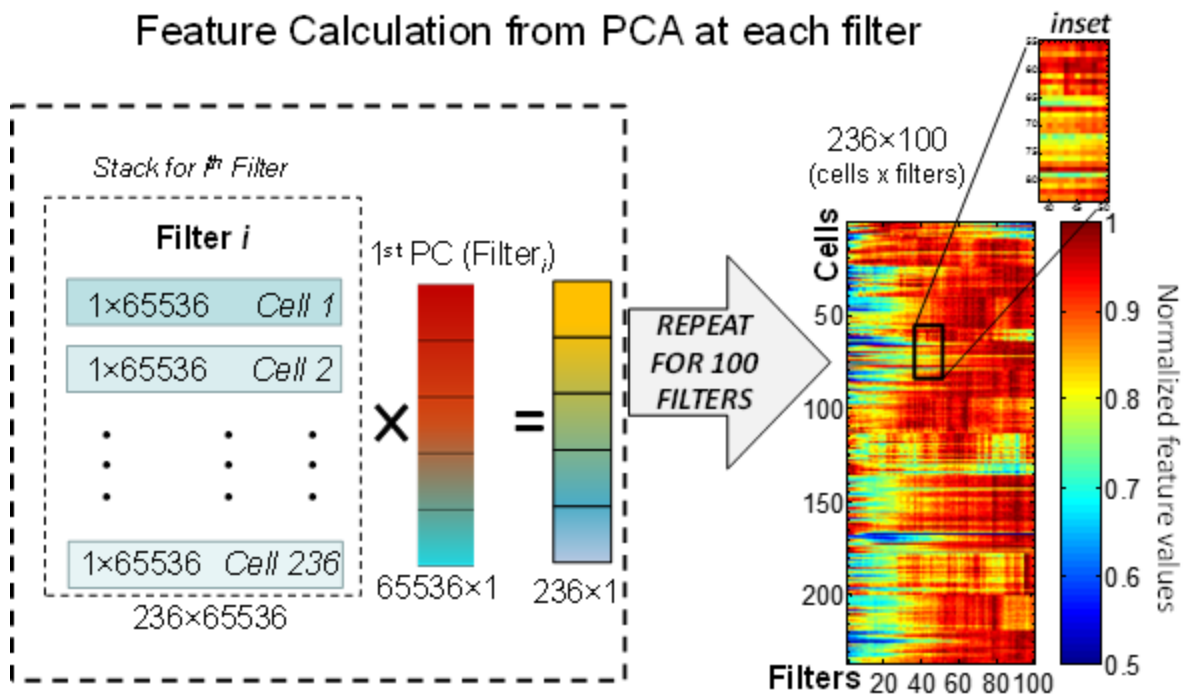


Figure 2-5 Generation of the Feature Matrix for cell classification. The reshaped $236 \times 65,536$ matrix which was used to perform the PCA at a given Gabor filter period (see also Figure 2-1) is reconsidered, and each row of the matrix (corresponding to each cell) is multiplied by the first principal component obtained from the PCA. This yields a scalar corresponding to each cell. A column of 236 scalars is therefore obtained at each Gabor

filter period. When all 100 filter periods are considered, a Feature Matrix of scalars with dimensions 236x100 is formed (False color image). The color scale corresponds to the Feature Matrix scalars normalized along each row by dividing the values in each row by the maximum value found for that same row. The data were normalized here for clarity of presentation. However, the classification was done using the raw values of the scalars obtained after the initial multiplication.

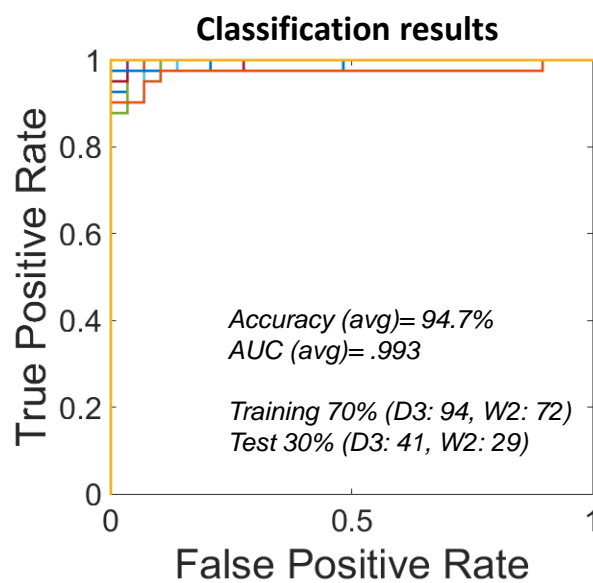


Figure 2-6 Receiver Operating Curves (ROC) obtained after classifying the Bax/Bak expressing cells (W2) and Bax/Bak double-knockout cells (D3). Using the Feature Matrix generated by the PCA, a supervised linear discriminant classifier was trained to differentiate the W2 from the D3 cells. The cell data were segregated into two groups: 70% of the cells were used for training, and 30% were used to test the classifier. The procedure was repeated 10 times, each time choosing the training and test groups randomly. The results show 10 overlapping ROC curves with an average area-under-the-

curve (AUC) of 0.993. The accuracy was taken as $(TP+TN) / (\text{Total number of cells})$. TP: True positives, TN: True negatives.

2.3.2.3 Identifying the most contributing structures (feature selection)

The feature selection algorithm was performed on the data sets using an increasing number of Gabor filter periods and calculating the MCE each time as described in Section 2.2.6. These results (Figure 2-7) demonstrate that 20 filters may provide a sufficiently low MCE and could be used instead of the full set of 100 filters for classifying the two cell variants. Hence, we performed this selection procedure 10 times (inset in Figure 2-7A) and the algorithm's 20 filter outputs were tallied in a histogram depicting the frequency with which a given filter appeared in the outputs of the 10 runs (Figure 2-7B). For our final selection, we only picked the 19 filters (listed in Figure 2-7B and Table 2-1) that appeared more than three times in the histogram. Utilizing only these 19 filters, we proceeded to re-classify the W2 and D3 cells. Figure 2-8 shows the classification results using the 19 filters selected in Figure 2-7B that yielded an average 89.8% accuracy and an average AUC of 0.956.

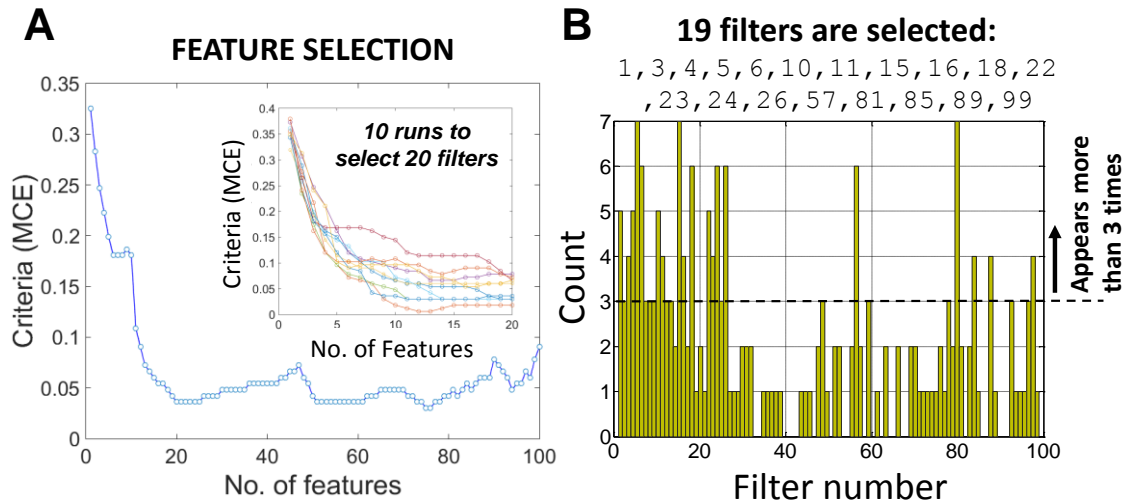


Figure 2-7 Feature Selection. A feature selection algorithm was implemented to find the Gabor filter periods (columns of the Feature Matrix in Figure 2-5) which are most significant to differentiate between the Bax/Bak expressing cells (W2) and the Bax/Bak double knockout cells (D3). A: The feature selection algorithm sequentially increased the number of Gabor filter periods included in the classification and calculates the misclassification error (MCE) as $(FP+FN) / (\text{Total number of cells})$. FP: False positives, FN: False negatives. The error is significantly decreased after including 20 filters. The feature selection algorithm was then run 10 times after setting the number of features to be used to 20 (inset in Panel A). B: Frequency of filters obtained after running the feature selection algorithm 10 times and specifying the number of filters to be used to 20. 19 filters appeared with a frequency of greater than 3 and were taken as representing the main structural feature sizes (see also Table 2-1) accounting for the differences between the classified W2 and D3 cells.

Table 2-1: Gabor filter periods associated with the 19 filters obtained from the feature selection step

Filter No.	1	3	4	5	6	10	11	15	16	18
Filter Period (μm)	2.93	2.53	2.37	2.23	2.10	1.72	1.64	1.39	1.34	1.25
Filter No.	22	23	24	26	57	81	85	89	99	
Filter Period (μm)	1.11	1.07	1.04	.99	0.54	0.40	0.39	0.37	0.34	

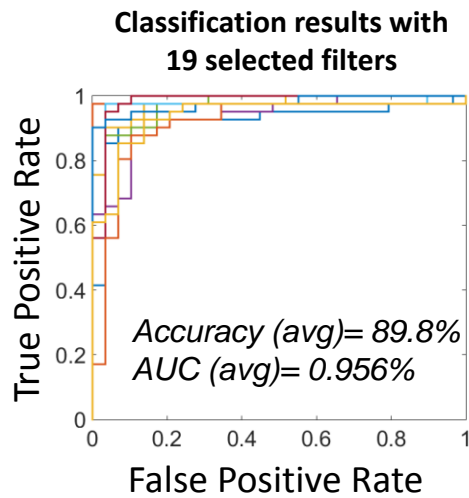


Figure 2-8 Classification results with selected filters. With the same procedure as in Figure 2-6, the classifier was rerun utilizing only the 19 filters found after feature selection (Refer to Figure 2-7). The new average AUC was 0.956 and the accuracy was 89.8%.

2.4 Discussion

In this work, we demonstrated how optical scatter imaging (OSI), a label-free method based on optical Fourier filtering of dark field images, can be combined with PCA and

discriminant analysis to differentiate, with greater than 95% accuracy, Bax/Bak double knockout iBMK cells from their Bax/Bak expressing counterparts. These results were obtained by finding principal components of the cell images (eigencell images) at each of the Gabor filter periods and constructing a Feature Matrix corresponding to the contribution that each cell makes to each of these eigencell Images. To a human observer, the two iBMK cell variants look qualitatively indistinguishable by DIC microscopy.

By utilizing a Feature Selection algorithm, we were able to identify the optical Gabor filter periods which contributed the most to the differences between the two cell variants. As shown previously²³, these Gabor filter periods scale linearly with the size of textural features within the sample. In our results (Figure 2-7B and Table 2-1) we found that filters with both large and small periods were necessary for successful classification of the two iBMK cell variants. This suggests that the genetic alteration in Bax and Bak can affect multiple subcellular components. In particular, the algorithm returned filter periods in the 2-3 μm , 1-1.5 μm , and 0.3-0.5 μm ranges, corresponding to features in the 1-1.5 μm , 0.5-0.75 μm and 0.15-0.25 μm ranges respectively²³. Previously, we had tested a limited number of iBMK cells and found that Gabor filters sensitive to the degree of orientation resulted in “orientedness”-encoded images with different histograms for Bax/Bak expressing and double knockout cells^{21, 22}. Those previous results were attributed to the differences in mitochondria found in Bax/Bak double knockout cells in which mitochondria are known to be shorter and less connected²⁵. Our results here, which corroborate the differences in subcellular architecture induced by the deletion of Bax/Bak, further suggest that the changes may not be limited to subcellular organelles

with sizes on the order of mitochondria but perhaps may also include differences in both larger and smaller components. Further work beyond the present study would require a more extensive analysis of isolated subcellular components (e.g. nucleus, mitochondria) to localize the source of the structural differences probed by the Gabor filters.

In contrast with our previous approaches in optical scatter imaging^{24, 26, 27}, the technique utilized here, creates eigencell images (Figure 2-4) that represent the spatial distribution of the principal cell features, and subsequently encodes the contribution of each cell to this eigencell image into a single scalar (by multiplying the cell vector by the eigencell vector, Figure 2-5). Rather than yielding a stack of false-color encoded images, which can be further processed, the technique presented here reduces the data set into a feature matrix akin to gene expression data. This procedure is also similar to the eigen-decomposition in face recognition^{28, 29}. In this approach, PCA of face images results in eigenvectors, also called “eigenfaces”, in which the intensity of each pixel is considered a characteristic feature, and describes the most informative regions of the face such as hair, eyes, mouth, nose etc. Similarly, the “eigencells” shown in Figure 2-4 display the subcellular elements that contribute the most throughout the size-encoded images at each Gabor filter period. For instance, the elements just outside the nuclear envelope are prominent in the PCs which correspond to Gabor filter periods under 2 μm . Statistical means such as Principal Component Analysis (PCA) for dimensionality reduction as well as feature extraction for further analysis have been employed abundantly in numerous fields including the life sciences; for example, to analyze thousands of gene expression data from hundreds of samples measured by DNA microarrays^{30, 31} or for the reconstruction of 3D structure of a single particle from a large collection of noisy 2D

tomographic projections by cryo-electron microscopy³². PCA is applied to compress the image representation as well as to reduce noise. Be it a set of 1D vectors of microarray data or a stack of 2D projection images, PCA reduces the dimensionality by calculating the eigenvectors of the covariance matrix of the data set and projecting each vector (or image) onto the linear subspace of the largest eigenvectors³³. These eigenvectors which are also called Principal Components (PCs) can be thought of as orthogonal directions along which the data has the highest variation. In this way, the PCs can be utilized to find discriminating features to classify specific cell types.

Light scattering techniques have been extensively applied to characterize cells undergoing various biological processes¹. Due to the noninvasive nature of these techniques, it is possible to monitor live cells in real-time. They also enable label-free detection and quantification of the structural dynamics specific to a biological process that can be used to infer important structure-function relationships at the cellular level. While fluorescence techniques could be superior at classifying cell types, the use of fluorescent labels may not always be feasible and label-free light scattering methods, such as OSI, may be desirable in these cases. In general, one reason for someone to adopt OSI, or an approach based on light scattering instead of fluorescence, is any situation where fluorescence labeling is not possible or impractical. One example is the cited light scattering techniques being developed to diagnose tissues in-vivo¹. In addition, compared with fluorescence, light scattering based methods do not require any sample preparation involving staining or transfection, and do not suffer from photobleaching. Other label-free methods such as evanescent wave microscopy technique to study membrane dynamics³⁴ or polarization diffraction flow cytometry to classify cell types

with similar morphology³⁵ may offer additional compelling approaches to study cellular function. However, at this point, it is not yet clear how or whether those methods will work to distinguish between cells of the exact same cell type, that differ by a single mutation and that are isogenic otherwise. On the other hand, we found that detecting such a genetic change is possible with OSI, which is what we are reporting here.

In our implementation, the OSI method consists of Fourier filtering by placing filters in a conjugate Fourier plane of an optical system. The filtering is automated and is not more tedious than acquiring a set of image frames while observing a sample. The PCA analysis is done offline after the acquisition. It is a standard signal processing technique with no significant added level of complexity compared to other biomedical image processing methods. In our current system which is software automated, we collect images at 5 fps and acquisition of 200 images takes approximately 40s. The PCA takes on average ~45s per stack. The time required to process one stack is approximately 45s using Matlab 2015(a) running on a workstation equipped with two Intel(R) Xeon(R) CPU, 2.67GHz processors but without utilizing GPU processing. The total time for PCA-based analysis of the whole data-set can be reduced in the future through parallel-processing in Matlab with the help of multicore processors (e.g. Matlab, Parallel Computing Toolbox™ (2016), The MathWorks, Inc). The information provided by OSI relies on filtering of angular scatter signal which can be collected in many different ways, including reflectance regimes which are typically used for in-vivo data acquisition. For example, back-reflectance signal can be filtered and analyzed in a similar way. Thus, while our current OSI setup would need to be modified for in vivo imaging, this modification is possible via any other optical set up design in which the angular scatter

signal can be measured and filtered. Moreover, the current OSI design may be readily usable for in vitro cell analysis of cells retrieved from patients. Single cell segmentation is not required unless single cell analysis is the end goal of the clinical technique. Cells could potentially be segmented automatically by employing commonly used image processing algorithms³⁶. In future, there is thus a scope for optimization of the current code which may include automatic segmentation and parallel-processing.

In the context of cancer, scatter techniques were capable of sensing nanoscale alterations due to genetic mutations in cells that appear morphologically normal¹⁶⁻¹⁸. The morphological sources responsible for these changes are beginning to be elucidated. For example, some investigators have identified cellular structures such as the cytoskeleton³⁷, nuclear size and crowding within a tissue⁴, chromatin condensation³⁸, or fractal organization of intracellular scatterers³⁹, as sources that could give rise to the light scattering differences observed in precancerous vs. normal cells. In our work, we had identified changes in mitochondrial morphology in apoptosis-resistant cells overexpressing Bcl-x_L²⁴. Still, a deeper understanding is required to tie the extensive available genetic and biochemical data on cancer biology to the structural physical phenotypes which can be measured by light scattering. In particular, while we know that fundamental molecular pathways are affected in cancer cells, we do not fully understand which of these molecular changes can lead to detectable structural changes. The present work contributes to this by demonstrating how a specific mutation in the apoptosis pathway (Bax/Bak deletion) can yield structural differences detectable by light scatter.

Acknowledgements

We thank Dr. E. White of the Rutgers CINJ for generously providing the iBMK cell variants used in this study. We also thank Dr. I. Androulakis at Rutgers for pertinent discussions regarding PCA as applied to our images, and O. Ipaye for help with cell segmentation. This work was partially supported by NSF grant DBI-0852857 and a grant from Charles and Johanna Busch Memorial Fund at Rutgers to NNB, and an NSF REU summer fellowship to MTG.

References

1. Backman, V. and H. K. Roy (2011). "Light-Scattering Technologies for Field Carcinogenesis Detection: A Modality for Endoscopic Prescreening." *Gastroenterology* 140(1): 35-41.
2. Backman, V., M. B. Wallace, L. T. Perelman, J. T. Arendt, R. Gurjar, M. G. Muller, Q. Zhang, G. Zonios, E. Kline, T. McGillican, S. Shapshay, T. Valdez, K. Badizadegan, J. M. Crawford, M. Fitzmaurice, S. Kabani, H. S. Levin, M. Seiler, R. R. Dasari, I. Itzkan, J. Van Dam and M. S. Feld (2000). "Detection of preinvasive cancer cells." *Nature* 406(6791): 35-36.
3. Bigio, I. J. (2012). "Real-time Pathology to Guide Breast Surgery: Seeing Alone Is Not Believing." *Clinical Cancer Research* 18(22): 6083-6085.
4. Bon, P., T. Barroca, S. Leveque-Fort and E. Fort (2014). "Label-free evanescent microscopy for membrane nano-tomography in living cells." *Journal of Biophotonics* 7(11-12): 857-862.
5. Boustany, N. N., S. A. Boppart and V. Backman (2010). *Microscopic Imaging and Spectroscopy with Scattered Light. Annual Review of Biomedical Engineering*, Vol 12. 12: 285-314.
6. Boustany, N. N., Y. C. Tsai, B. Pfister, W. M. Joiner, G. A. Oyler and N. V. Thakor (2004). "BCL-x(L)-dependent light scattering by apoptotic cells." *Biophysical Journal* 87(6): 4163-4171.
7. Crescenzi, M. and A. Giuliani (2001). "The main biological determinants of tumor line taxonomy elucidated by a principal component analysis of microarray data." *Febs Letters* 507(1): 114-118.
8. Damania, D., H. K. Roy, H. Subramanian, D. S. Weinberg, D. K. Rex, M. J. Goldberg, J. Muldoon, L. Cherkezyan, Y. J. Zhu, L. K. Bianchi, D. Shah, P. Pradhan, M. Borkar, H. Lynch and V. Backman (2012). "Nanocytology of Rectal Colonocytes to Assess Risk of Colon Cancer Based on Field Cancerization." *Cancer Research* 72(11): 2720-2727.
9. Damania, D., H. Subramanian, V. Backman, E. C. Anderson, M. H. Wong, O. J. T. McCarty and K. G. Phillips (2014). "Network signatures of nuclear and cytoplasmic

density alterations in a model of pre and postmetastatic colorectal cancer." *Journal of Biomedical Optics* 19(1): 016016.

10. Degenhardt, K., G. Chen, T. Lindsten and E. White (2002a). "Bax and Bak mediate p53-independent suppression of tumorigenesis." *Cancer Cell* 2: 193-203.

11. Feng, Y. M., N. Zhang, K. M. Jacobs, W. H. Jiang, L. V. Yang, Z. G. Li, J. Zhang, J. Q. Lu and X. H. Hu (2014). "Polarization Imaging and Classification of Jurkat T and Ramos B Cells Using a Flow Cytometer." *Cytometry Part A* 85A(9): 817-826.

12. Frank, J. (2006). *Three-dimensional electron microscopy of macromolecular assemblies. Three-dimensional electron microscopy of macromolecular assemblies: visualization of biological molecules in their native state.* New York, NY, Oxford University Press.

13. Greiner, C., M. Hunter, P. Huang, F. Rius and I. Georgakoudi (2011). "Confocal Backscattering Spectroscopy for Leukemic and Normal Blood Cell Discrimination." *Cytometry Part A* 79A(10): 866-873.

14. Hanahan, D. and R. A. Weinberg (2011). "Hallmarks of Cancer: The Next Generation." *Cell* 144(5): 646-674.

15. Jolliffe, I. T. (2002). *Principal component analysis, Second Edition.* New York, NY, Springer.

16. Karbowski, M., K. L. Norris, M. M. Cleland, S.-Y. Jeong and R. J. Youle (2006). "Role of Bax and Bak in mitochondrial morphogenesis." *Nature* 443: 658-662.

17. Kim, J. S., P. Pradhan, V. Backman and I. Szeifer (2011). "The influence of chromosome density variations on the increase in nuclear disorder strength in carcinogenesis." *Physical Biology* 8(1): Article # 015004.

18. Liu, Y., R. E. Brand, V. Turzhitsky, Y. L. Kim, H. K. Roy, N. Hasabou, C. Sturgis, D. Shah, C. Hall and V. Backman (2007). "Optical markers in duodenal mucosa predict the presence of pancreatic cancer." *Clinical Cancer Research* 13(15): 4392-4399.

19. Meijering, E. (2012). "Cell Segmentation: 50 Years Down the Road." *IEEE Signal Processing Magazine* 29(5): 140-145.

20. Misra, J., W. Schmitt, D. Hwang, L. L. Hsiao, S. Gullans, G. Stephanopoulos and G. Stephanopoulos (2002). "Interactive exploration of microarray gene expression patterns in a reduced dimensional space." *Genome Research* 12(7): 1112-1120.

21. Mourant, J. R., I. J. Bigio, J. Boyer, R. L. Conn, T. Johnson and T. Shimada (1995). "Spectroscopic diagnosis of bladder cancer with elastic light scattering." *Lasers in Surgery and Medicine* 17(4): 350-357.

22. Mutyal, N. N., A. Radosevich, A. K. Tiwari, Y. Stypula, R. Wali, D. Kunte, H. K. Roy and V. Backman (2013). "Biological Mechanisms Underlying Structural Changes Induced by Colorectal Field Carcinogenesis Measured with Low-Coherence Enhanced Backscattering (LEBS) Spectroscopy." *Plos One* 8(2): Article Number e57206.

23. Pasternack, R. M., Z. Qian, J. Zheng, D. N. Metaxas, E. White and N. N. Boustany (2008). "Measurement of Subcellular Texture by Optical Fourier Filtering with a Micromirror Device." *Optics Letters* 33(19): 2209-2211.

24. Pasternack, R. M., Z. Qian, J. Zheng, D. N. Metaxas, E. White and N. N. Boustany (2009). "Measurement of Subcellular Texture by Optical Fourier Filtering with a Micromirror Device- ERRATUM." *Optics Letters* 34: 1939.

25. Pasternack, R. M., J. Zheng and N. N. Boustany (2011). "Detection of Mitochondrial Fission with Orientation-Dependent Optical Fourier Filters." *Cytometry, Part A* 79A: 137-148.
26. Perelman, L. T., V. Backman, M. Wallace, G. Zonios, R. Manoharan, A. Nusrat, S. Shields, M. Seiler, C. Lima, T. Hamano, I. Itzkan, J. V. Dam, J. M. Crawford and M. S. Feld (1998). "Observation of periodic fine structure in reflectance from biological tissue: A new technique for measuring nuclear size distribution." *Physical Review Letters* 80(3): 627-630.
27. Qiu, L., D. K. Pleskow, R. Chuttani, E. Vitkin, J. Leyden, N. Ozden, S. Itani, L. Y. Guo, A. Sacks, J. D. Goldsmith, M. D. Modell, E. B. Hanlon, I. Itzkan and L. T. Perelman (2010). "Multispectral scanning during endoscopy guides biopsy of dysplasia in Barrett's esophagus." *Nature Medicine* 16(5): 603-607.
28. Rodriguez-Diaz, E., C. S. Huang, A. Sharma, L. I. Jepeal, I. J. Bigio and S. K. Singh (2012). "Optical Sensing of Field Carcinogenesis in Colonic Mucosa Using Elastic-Scattering Spectroscopy (ESS)." *Gastroenterology* 142(5): S110-S110.
29. Sierra, H., J. Y. Zheng, B. Rabin and N. N. Boustany (2012). "Measurement of object structure from size-encoded images generated by optically-implemented Gabor filters." *Optics Express* 20(27): 28698-28706.
30. Sirovich, L. and M. Kirby (1987). "Low-Dimensional Procedure for the Characterization of Human Faces " *Journal of the Optical Society of America a-Optics Image Science and Vision* 4(3): 519-524.
31. Subramanian, H., P. Pradhan, Y. Liu, I. R. Capoglu, X. Li, J. D. Rogers, A. Heifetz, D. Kunte, H. K. Roy, A. Taflove and V. Backman (2008). "Optical methodology for detecting histologically unapparent nanoscale consequences of genetic alterations in biological cells " *Proceedings of the National Academy of Sciences of the United States of America* 105(51): 20118-20123.
32. Terry, N., Y. Z. Zhu, J. K. M. Thacker, J. Migaly, C. Guy, C. R. Mantyh and A. Wax (2011). "Detection of intestinal dysplasia using angle-resolved low coherence interferometry." *Journal of Biomedical Optics* 16(10): 6.
33. Turk, M. and A. Pentland (1991). "Eigenfaces for Recognition " *Journal of Cognitive Neuroscience* 3(1): 71-86.
34. Vogelstein, B., E. R. Fearon, S. R. Hamilton, S. E. Kern, A. C. Preisinger, M. Leppert, Y. Nakamura, R. White, A. M. M. Smits and J. L. Bos (1988). "Genetic Alterations During Colorectal-Tumor Development." *New England Journal of Medicine* 319(9): 525-532.
35. Vogelstein, B. and K. W. Kinzler (2004). "Cancer genes and the pathways they control." *Nature Medicine* 10(8): 789-799.
36. Vogelstein, B., N. Papadopoulos, V. E. Velculescu, S. B. Zhou, L. A. Diaz and K. W. Kinzler (2013). "Cancer Genome Landscapes." *Science* 339(6127): 1546-1558.
37. Wax, A., N. G. Terry, E. S. Dellon and N. J. Shaheen (2011). "Angle-Resolved Low Coherence Interferometry for Detection of Dysplasia in Barrett's Esophagus." *Gastroenterology* 141(2): 443-447.
38. Zheng, J., Y. Tsai, P. Kadimcherla, R. Zhang, J. Shi, G. A. Oyler and N. N. Boustany (2008). "The C-terminal transmembrane domain of Bcl-xL mediates changes in mitochondrial morphology." *Biophysical Journal* 94(1): 286-297.

39. Zhu, Y. Z., N. G. Terry and A. Wax (2012). "Angle-resolved low-coherence interferometry: an optical biopsy technique for clinical detection of dysplasia in Barrett's esophagus." *Expert Review of Gastroenterology & Hepatology* 6(1): 37-41.

CHAPTER 3

3 LABEL-FREE DYNAMIC SEGMENTATION AND MORPHOLOGICAL ANALYSIS OF SUBCELLULAR OPTICAL SCATTERERS

This chapter includes work published in Mohammad Naser, Rene S. Schloss, Pauline Berjaud, Nada N. Boustany, “Label-Free Dynamic Segmentation and Morphological Analysis of Subcellular Optical Scatterers”, *Journal of Biomedical Optics* (In Press), with permission.

Abstract

Imaging without fluorescent protein labels or dyes presents significant advantages for studying living cells without confounding staining artifacts, and with minimal sample preparation. Here, we combine label-free Optical Scatter Imaging (OSI) with digital segmentation and processing to create dynamic subcellular masks, which highlight significantly scattering objects within the cells’ cytoplasm. The technique is tested by quantifying organelle morphology and redistribution during cell injury induced by calcium overload. Objects within the subcellular mask are first analyzed individually. We show that the objects’ aspect ratio and degree of orientation (“Orientedness”) decrease in response to calcium overload, while they remain unchanged in untreated control cells. These changes are concurrent with mitochondrial fission and rounding observed by fluorescence, and are consistent with our previously published data demonstrating scattering changes associated with mitochondrial rounding during calcium injury. In addition, we show that the magnitude of the textural features associated with the spatial

distribution of the masked objects' orientedness values, changes by more than 30% in the calcium-treated cells compared with no change or changes of less than 10% in untreated controls, reflecting dynamic changes in the overall spatial distribution and arrangement of subcellular scatterers in response to injury. Taken together, our results suggest that our method successfully provides label-free morphological signatures associated with cellular injury. Thus, we propose that dynamically segmenting and analyzing the morphology and organizational patterns of subcellular scatterers as a function of time, can be utilized to quantify changes in a given cellular condition or state.

3.1 Introduction

Live cell imaging is crucial to understand the biological functions of a cell and its organelles. Fluorescent imaging has been a gold standard in this regard. While fluorescent stains provide good specificity and contrast, they also present some shortcomings including photo-bleaching and photo-toxicity¹. In addition, cell transfection with fluorescent protein constructs, and sample staining, may complicate sample preparation or interfere with cell function and confound the results². To circumvent these shortcomings of imaging with fluorescent markers, label-free techniques, which do not require any stains or markers are currently being developed³⁻⁵.

Here, we utilize an optical scatter imaging (OSI) method based on dark-field microscopy and angular light scattering that is capable of tracking the distribution and morphology of subcellular structures, such as organelles, as a function of time. Imaging based on light scattering has previously enabled label-free detection and quantification of subcellular structural properties and dynamics pertaining to a biological process without

the use of any exogenous marker⁶. For example, wavelength and angularly-resolved scattering was used to extract nuclear size information^{7,8}. Wilson et al. used angularly-resolved light-scattering measurements to detect mitochondrial swelling upon photodynamically induced oxidative stress⁹. Light-scattering by various mitochondrial distributions has been studied with a finite-difference time-domain (FDTD) simulation, which was applied to differentiate between cancerous cells with randomly distributed mitochondria and healthy cells with aggregated mitochondria around the nucleus¹⁰. In addition, we have previously utilized the ratio of wide-to-narrow angle scatter measurements to track calcium-induced mitochondrial injury¹¹ and apoptosis¹². This previously reported OSI method employs optical Fourier-filtering at a conjugate Fourier plane of the imaging system. More recently, via implementation of Gabor filters on the Fourier plane, we were able to probe objects of different size/shape and orientation^{13,14}. Based on this method, one morphometric parameter, termed Orientedness, which probes the geometric aspect ratio of subcellular organelles was shown to be sensitive to the morphological changes related to mitochondrial fission during apoptosis in Bovine Aortic Endothelial Cells (BAEC)¹⁴.

In this paper, we build upon our previous results by applying edge detection¹⁵ and segmentation¹⁶ methods to our filtered dark-field image data. Together, these methods allow us to amplify the signal from highly scattering subcellular structures relative to background, as well as segment these highly scattering microscopic regions within the cell cytoplasm. Combining these steps together, we develop an approach that can track subcellular dynamics non-invasively, in unstained cells over time. As a test of this method, we apply this approach to quantify morphological changes governed by

mitochondrial fragmentation and remodeling induced by calcium overload. We demonstrate that the morphological signatures generated from unstained cells can clearly differentiate between injured and untreated cells.

3.2 Methods

3.2.1 Cell culture

Bovine Aortic Endothelial Cells (BAEC) were cultured on glass coverslips as previously described¹⁴. To compare the dark-field data with fluorescence imaging, For fluorescence labeling, cells were incubated in HEPES Buffered balanced Salt Solution (HBSS)¹¹ supplemented with 100nM Mitotracker Green (Invitrogen) for 45min following the manufacturer's protocol. The cover-slips containing the cells were mounted on a metal-slide for imaging as described in Ref. 14.

3.2.2 Calcium treatment

To induce subcellular morphological change, the cells were overloaded with calcium via treatment with ionomycin (Sigma-Aldrich), a calcium ionophore. Pre-treatment imaging was conducted in a salt-solution¹¹ containing 1.5mM CaCl₂. The treatment solution was prepared by adding 20μM ionomycin to the same saline medium. To induce the calcium overload, the chamber containing the cells was flushed three times with this treatment solution. Taking this point as $t=0$, time-lapse post-treatment images were collected every 45s for a maximum of 10min. For control, a 1.5mM CaCl₂ with no ionomycin was flushed three times instead of the treatment solution.

3.2.3 Optical setup and image acquisition

Details of the optical setup are described in Ref. 13 and shown in Figure 3-1. Briefly, an inverted microscope fitted with a 63X, N.A. = 1.4 oil immersion objective is used to image the sample illuminated with a laser at $\lambda=532\text{nm}$. The incident laser light is passed through a spinning diffuser to average speckle. Scattered light from the sample is filtered by displaying images of Gabor filters on a Liquid Crystal Display (LCD) placed in a conjugate Fourier plane (F_2). The resulting filtered images are captured by a CCD camera placed in a conjugate imaging plane (I_2).

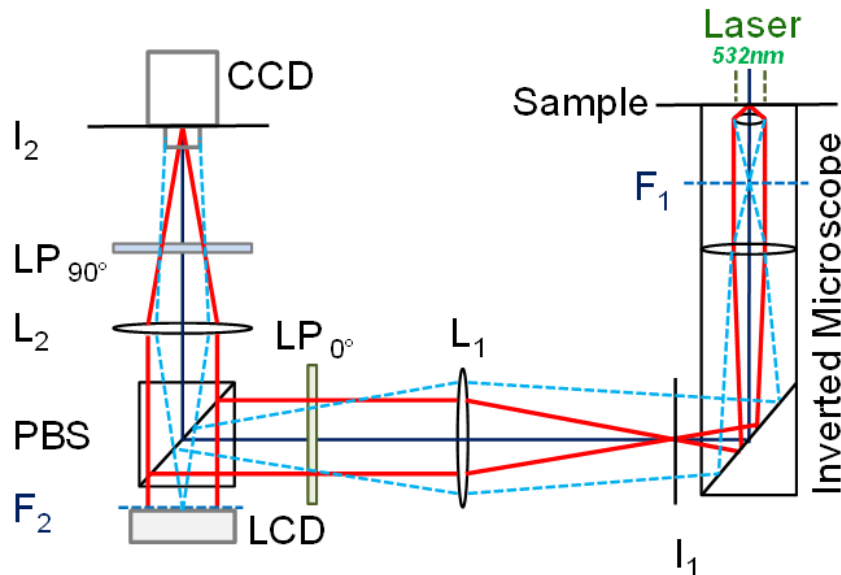


Figure 3-1 Optical setup. The OSI technique involves the acquisition of dark-field, filtered images on the charge-coupled device (CCD) camera. Two-dimensional (2D) Gabor filters are displayed on a Liquid Crystal Device (LCD) in the Fourier plane. L_1 and L_2 : relay lenses, PBS: polarizing beam splitter, LP= linear polarizer, F_1 and F_2 : conjugate Fourier planes, I_1 and I_2 : conjugate imaging planes.

3.2.4 Gabor filter design

The Gabor filter images displayed on the LCD are created in Matlab (The Mathworks, Natick, MA). In the object or image space, the filters are characterized by three parameters: period (S), orientation (φ) and standard deviation (σ_{space}). While deviation determines the size of the object area probed by the Gabor filter, the period and standard deviation are typically chosen to not be independent¹⁶ so that the region probed by the filter scales with the filter's period. For this work we choose $\sigma_{space} = \frac{S}{2}$, and we choose 6 periods, S (in μm) = 2.0, 1.43, 1.11, 0.91, 0.77, 0.66, and 4 orientations $90^\circ \leq \varphi < 225^\circ$ with 45° increment. To implement the filters in a conjugate Fourier plane, we convert these parameters to their frequency domain equivalents within the actual optical setup. The period transforms to the spatial frequency, $F = \frac{1}{S}$ and $\sigma_{frequency} = \frac{1}{2\pi\sigma_{space}}$ ¹⁷.

The filters are created in Matlab by defining a Gaussian function as shown below. Derivation of the equation is shown in Table 3-1 (see Appendix).

$$H(u, v) = A * e^{-\frac{\pi^2}{2*(U^2+V^2)}[(u-U)^2+(v-V)^2]}$$

A is set to 255, and (U, V) are the coordinates in Fourier space and are calculated by:

$$U = F * \cos\varphi \text{ and } V = F * \sin\varphi$$

To calibrate for spatial frequency, a diffraction pattern with known spatial frequency spacing is used as described in Ref. 13. The calibration factor for the current setup is 0.0075 cycles/ μm /LCD-pixel and the distance, F , of the Gaussian-peaks from the center of the LCD can be calculated using this factor. We also correct for the LCD's reflectance by correcting the Gaussian's gray scale values using the LCD's measured look-up-table (LUT) which gives the LCD reflectance as a function of gray scale input. As such, the

gray scale values inputted into the LCD will result in the expected Gaussian-shaped reflectance. Since, the Fourier transform of a Gabor function is a center-shifted Gaussian; the filters are realized by placing the peaks of the Gaussians at a distance F from the center of the LCD. The coordinates of these pixels correspond to the spatial frequencies whose inverse correspond to the pre-chosen periods.

Once the filtered-images are captured in the CCD, they are further processed as shown in Figure 3-2. To generate the Orientedness images, local energy is calculated at each pixel first. Orientedness images are then masked using the dynamic masks generated using the maximum moment of phase-congruency images. Finally, features are extracted from both the binary masks, and the masked-Orientedness images. Calculation of local energy, Orientedness, and phase-congruency are described in the following sections.

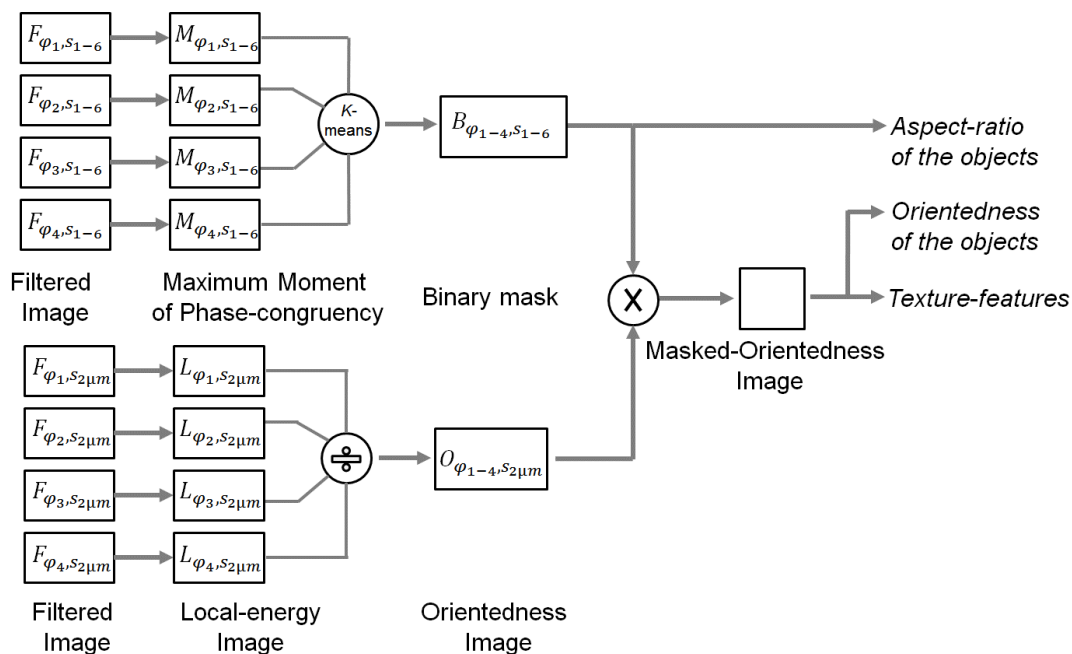


Figure 3-2 Flow-chart of the algorithm utilized for image analysis.

3.2.5 Generating local energy and phase congruency (maximum moment) images

In one dimension, phase-congruency is defined as $PC(x) = \frac{|E(x)|}{\sum_n A_n(x)}$ where $A_n(x)$ are the amplitudes of n Fourier components at a location (x), and local energy $E(x)$ is the vector summation of all components¹⁵. Phase-congruency acts as a highly localized operator to detect edges and corners in an image that is invariant to illumination and magnification. This technique takes advantage of the fact that Fourier components of the edge- or corner-points in an image are maximally in phase. This can be explained by a simple example of a square pulse. If all of the Fourier components of the square pulse are superimposed on each other, it can be shown that all of them will be in phase at the edges of the pulse. Thus for the edge, the summation of the component-amplitudes is equal to the vector summation of all components, producing a PC value of 1. A minimum value of 0 may be obtained if all of the components are out of phase. Kovési proposed to extract the frequency information via wavelet transform instead of taking the Fourier transform¹⁵. The wavelet transform is realized by even and odd symmetric Log-Gabor filters of varying scale and orientation. Using the phase-congruency information, the edge-like features in the subcellular domain are then enhanced by taking the maximum moment of the phase-congruency covariance matrix. In this work, we have used an optimized code-version developed by Kovési¹⁸ to generate the maximum moment and local energy images from each of the Gabor filtered images acquired in the set up. Thus, for each sample, 24 maximum moment images and 24 local energy images are calculated from the 24 optically filtered images acquired by the setup. These images are obtained from the ‘M’ and ‘pcSum’ variables found in the abovementioned code.

In addition, the user may set several input parameters pertaining to the calculation of phase congruency. In particular, the local frequency information is obtained via digital Log-Gabor wavelets of different scales and orientations. In this work, we set the number of scales ('nscale' in the code) to 4 and number of orientations ('norient') to 4. We set the minimum wavelength of the wavelet ('minWaveLength') to 2 pixels and the scaling between successive wavelengths ('mult') to 2.1. Hence for 4 scales we obtain wavelets with wavelengths 2, 4.2, 8.82 and 18.5 pixels. To detect spatial properties at different orientations, 4 angles from 0° to 135° spaced 45° apart are used. The width of the filter function is controlled by the angular standard deviation σ_G of the function that is dependent on the filter center frequency, f_o as $R = \frac{\sigma_G}{f_o}$. We set $R = 0.65$ for this work (R corresponds to 'sigmaOnf' in the code). Such combination of the scaling factor and R ensures an even coverage of the spectrum. Finally, we set 'k' = 1, 'cutoff' = 0.5 and 'gamma' (gain) = 5. As described in Ref. 15, the code utilizes a weighting function that penalizes any phase-congruency value that is not spread beyond a certain frequency. This is because phase-congruency is significant only when it occurs over a wide range of frequencies. This function is of sigmoid form and can be controlled by two parameters: cutoff fraction which dictates the amount of frequencies considered for the phase-congruency to be significant, and gain (gamma) which controls the steepness of the sigmoid function. In addition, 'k' corresponds to the number of standard deviations of the noise energy beyond the mean at which the noise threshold is set. Only signal energies beyond this threshold will be considered. For noisy images, the value of 'k' can be set up to 20. However this will increase the threshold and result in loss of useful data. In our

case, we set the value as low as 1 to avoid any such loss while discarding a minimum level of noise.

3.2.6 Generating Orientedness images

Orientedness is a scattering-based parameter we had previously defined as the maximum signal over the average signal collected as a function of orientation,

$$= \frac{\max(\text{Signal}, \varphi_i)}{\langle \text{Signal}, \varphi_i \rangle} \Big|_{S=0.9\mu},$$

and taken for data filtered with a Gabor period of $0.9\mu\text{m}^{11}$. φ_i is the orientation of the Gabor filters used in the experimental setup. For a round object, there will be an equal amount of scattering in all φ , resulting a minimum Orientedness value of 1; whereas for an elongated object, the scatter profile will be oriented in a certain direction, producing an Orientedness value greater than 1. As shown previously¹¹, Orientedness decreases as long mitochondria fragment and round upon injury. In this work, we calculated Orientedness using the local energy images, defined in the previous section, instead of the raw intensity values $\{\text{signal}, \varphi_i\}$. Here, $90^\circ \leq \varphi_i < 225^\circ$, and the optically filtered images with a Gabor filter period of $2\mu\text{m}$ were used in this calculation.

Hence, the modified equation is given by $Orientedness = \frac{\max(\text{local energy}, \varphi_i)}{\langle \text{local energy}, \varphi_i \rangle} \Big|_{S=2\mu}$.

3.2.7 Image segmentation

First, the nucleus regions as well as the background outside the cells (no-cell region) are segmented out manually from the cell images so as to only analyze the scatters within the cytoplasm. Then, following the main frame-work proposed by Jain et al¹⁶, each Gabor-filtered image is pre-processed and fed to a clustering algorithm. However, we applied phase-congruency as a pre-processing step instead of the ‘‘blob-detection’’ approach applied in Ref. 16. Thus, pixels in the maximum moment images obtained above are

subjected to a k -means clustering algorithm which groups them into 4 clusters according to their intensities in the 24 optically filtered images. We found 4 to be the highest number of clusters to be used for these images as the algorithm does not converge for a greater number of clusters. Pixels categorized in each cluster are color-labeled with one of the 4 colors: blue, turquoise, yellow and red. In this analysis, all the experimental timepoints for a given cell were analyzed at once, yielding 4 classes evolving as a function of time.

3.3 Results

3.3.1 Cell images produced by the algorithm

Images obtained at different steps are shown in Figure 3-3. The Gabor-filtered image is obtained with $S=2.0\mu\text{m}$, $\varphi=225^\circ$ and the corresponding phase-congruency (maximum moment), local-energy, and Orientedness images are shown. The dark-field image is also shown. The dark-field image contains all spatial-frequency components; hence it contains the scattering information from objects of all sizes and orientations. On the other hand, it is mostly the objects oriented at 225° that are highlighted in the Gabor-filtered image. Enhanced edges of these objects can be seen in the maximum moment image. The Orientedness image maps the Orientedness values of the subcellular objects in the cytoplasm. As indicated by the colorscale, objects with a hue toward the blue have low Orientedness and hence are round compared to the objects shown in red.

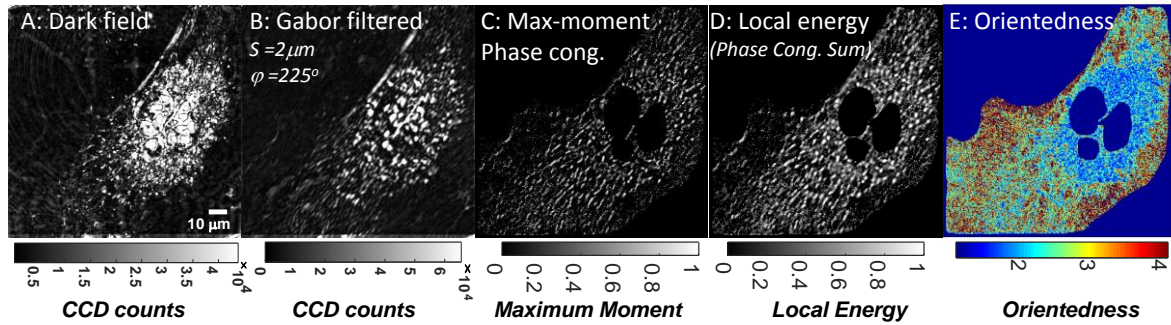


Figure 3-3 Dark-field (A), Gabor-filtered ($S=2.0$, $\phi=225^\circ$) (B), phase-congruency (maximum moment) (C) Local Energy (D), and Orientedness (E) images of a representative cell. Note, edges are enhanced in the phase-congruency (maximum moment) image.

3.3.2 Tracking subcellular organelles with dynamic masking

To segment the subcellular objects in the cytoplasm, we applied a K-means algorithm to classify the pixels in the maximum moment images. Before classification, the data is standardized by subtracting the mean and dividing by the standard deviation to obtain zero mean and unit variance. Figure 3-4 shows the 4 colored pixel clusters resulting from the K-means algorithm for a representative cell. To verify whether the clusters contain pixels with significant morphological information as well as to discard clusters that contain pixels from the background, we analyze the 4 centers, or centroids, of the 4 clusters (Figure 3-5A). Each centroid has 24 centroid components, representative of the 24 filtered intensities of pixels within the cluster associated with that centroid. The 24 centroid values are arranged as a function of optical filter period, S , and orientation ϕ . As can be seen in the polar-plots (Figure 3-5A), the centroid values of the turquoise (Cluster 2) and red labels (Cluster 4) vary as a function of period and orientation. On the other hand, there no or little change in the centroid values for blue (Cluster 1) and yellow labels

(Cluster 3). The blue and yellow clusters also have lower values. This indicates that the pixels from these two clusters are either from the background outside the cell or the nuclei which were manually segmented out (Blue in Figure 3-4), or subcellular regions with significantly less intensity than the red and turquoise regions (Yellow in Figure 3-4). We quantified the variation in cluster values by taking the magnitude (*mag*) of each cluster, where $mag = \sqrt{\sum_{S,\varphi} c^2}$ and c is the centroid-value corresponding to a filter (S, φ). The bigger the magnitude, the greater the variation over period and orientation. We then pick two clusters with the highest magnitudes and add them to create a single binary mask for the pre-treatment condition (Figure 3-5B). Keeping the selected clusters the same, we repeat the combining process for each time point of data acquisition to generate masks that change over the period of time. We then create “masked orientedness” images by multiplying the Orientedness images with the binary masks at each time point (Figure 3-6).

As can be seen in Fig. 6, dynamic masks created by the proposed algorithm change shape over time as the cell shrinks upon severe chemical insult (Figure 3-7). Most of the long objects in the masks become fragmented or round along with the cell-shrinkage, and exhibit a decrease in their orientedness value. Concurrently, mitochondria become shorter and rounder upon calcium-overloading, observed in the MitoTracker labeled fluorescent images (Figure 3-8).

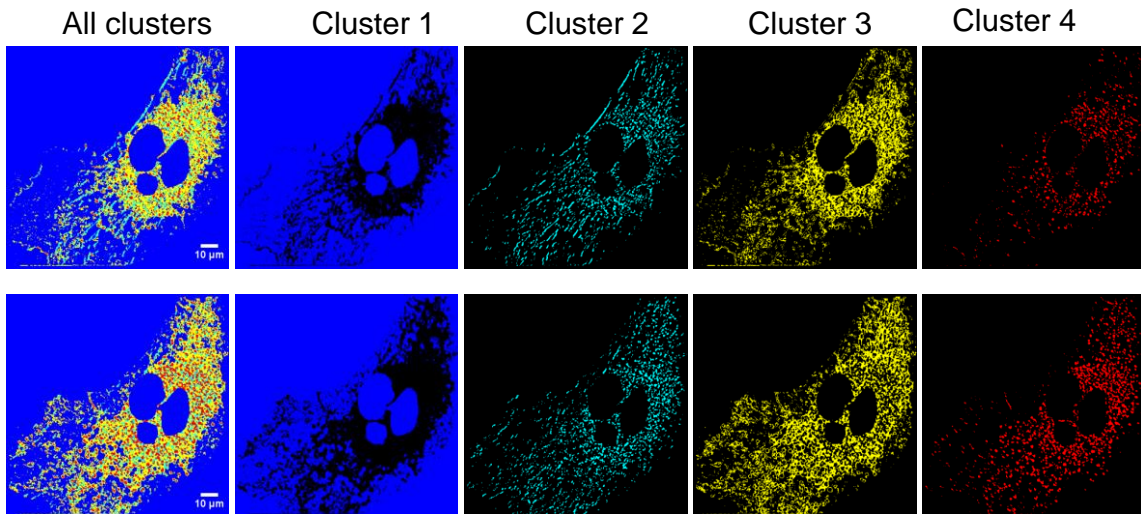


Figure 3-4 Four pixel clusters labeled in blue, turquoise, yellow and red. Top panels: pre-treatment, and bottom panels: post-treatment. Each of these clusters contains objects with different scattering profiles and intensities. Note also how the shape of the labeled objects changes with treatment; particularly elongated objects in the turquoise-cluster become smaller and rounder.

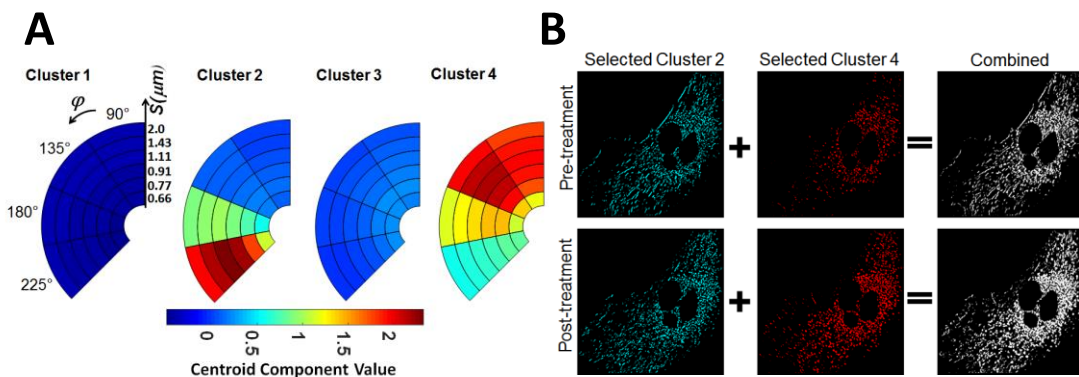


Figure 3-5 Color-coded centroid values are arranged in a 4x6 polar plot corresponding to 4 orientations and 6 periods for each label shown in Figure 3-4. In both pre- and post-treatment cases, the centroid components of the turquoise and red clusters' demonstrate variation over orientations (ϕ) as well as periods (S), while those of the blue

and yellow clusters have low signal with little or no variation. B: The turquoise and red clusters are added together to produce a combined final binary mask.

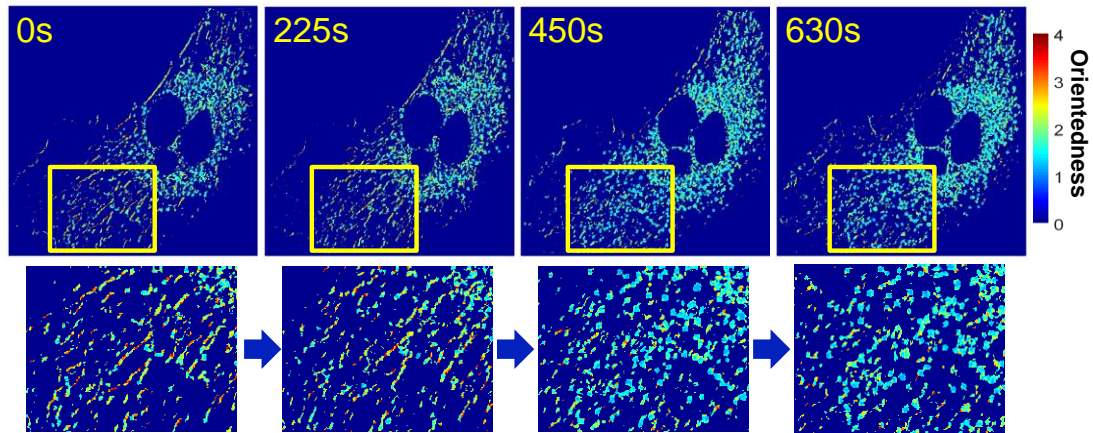


Figure 3-6 Masked Orientedness image of a representative cell. Gradual change in the subcellular scatterers and shape of the dynamic mask can be observed upon injury at $t=0$.

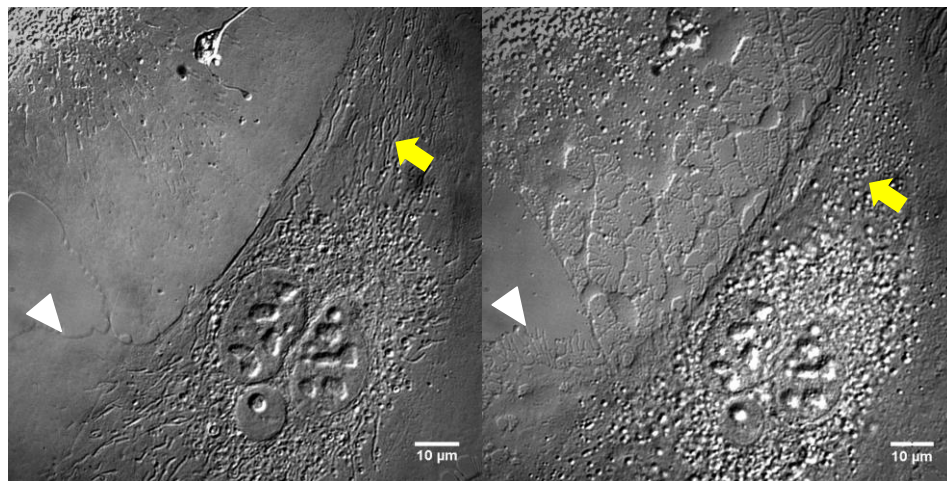


Figure 3-7 Differential interference contrast (DIC) image of a cell undergoing calcium-overloading. Long objects (arrow) observed in the pre-treatment image (left) fragment and become round due to excessive calcium (right). The cell also shrinks which

is indicated by trace-marks of the cell membrane (arrow-head). When compared with MitoTracker labeled fluorescent images, the fragmented and rounded long objects in the DIC images correspond to mitochondria (Figure 3-8).

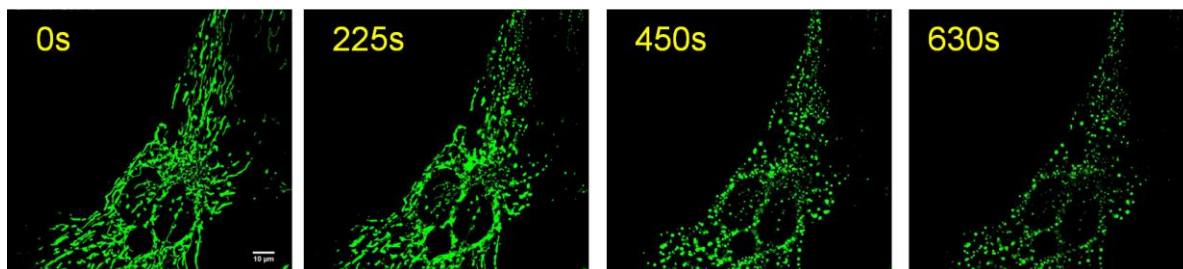


Figure 3-8 MitoTracker labeled fluorescent images show mitochondrial fragmentation and remodeling upon calcium-overloading.

3.3.3 Effect of Jain's multi-channel filtering approach

Jain's framework is based on a multi-channel filtering approach, originally proposed in Ref. 19, which dictates that the human visual system decomposes retinal information into a number of filtered images. The 'multi-channels' are realized by the Gabor filters. To understand the effect of Gabor-filters on the final segmented image with classified pixels, we applied phase-congruency and clustering of the pixels on the unfiltered dark-field image. Segmented images obtained using the single-channel (DF only) and Multi-channel (Gabor) contain almost the same information in the cellular region, except the former has noise (Figure 3-9). The multi-channel approach decomposes the same information of the dark-field into multiple channels and allows selecting the channels less corrupted by noise. Hence we can discard the channels manually (i.e. Gabor filters of particular period and orientation) that are corrupted by noise. This enabled us to generate a cleaner image

compared to that obtained by using dark-field only. Similarly, other “single-channel” label-free images such as the DIC image can be used to generate the Segmented image, but like dark-field image they also might contain redundant information.

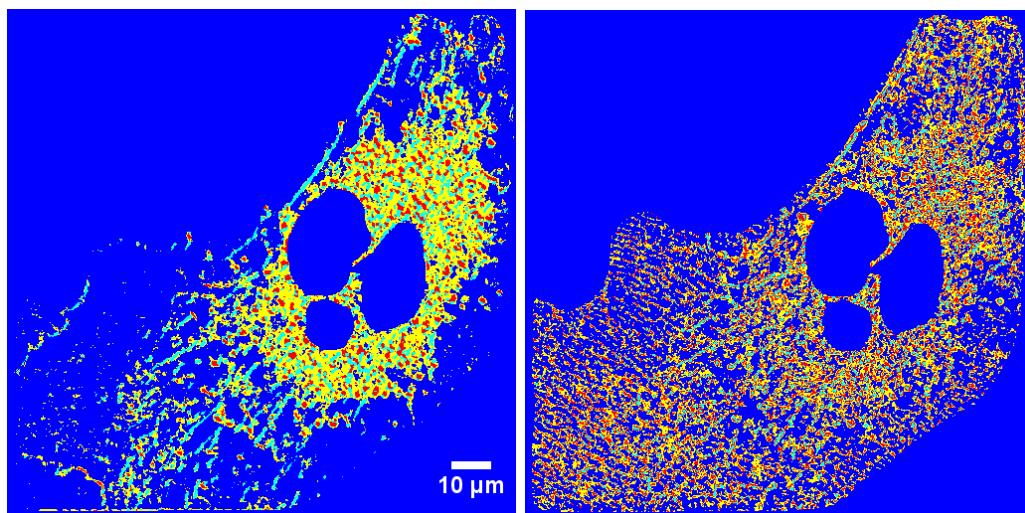


Figure 3-9 Classified images generated using the multi-channel Gabor-filtered images (left) and the single unfiltered dark-field image (right).

3.3.4 Aspect-ratio and Orientedness decrease upon injury

To quantify the subcellular morphological changes, we analyzed the subcellular objects segmented by the image masks obtained above (Figure 3-5). Objects are defined as clusters of pixels with connectivity with 4 pixels²⁰. We measured the aspect-ratio of the objects over time to quantify the subcellular morphological changes (Figure 3-10A). We also calculated the median Orientedness from the pixels contained in each object. Figure 3-10B shows that the object’s median orientedness decreases upon cell injury. Analysis of the aspect ratio of the mito-tracker labeled objects also shows a simultaneous decrease with treatment (Figure 3-10C).

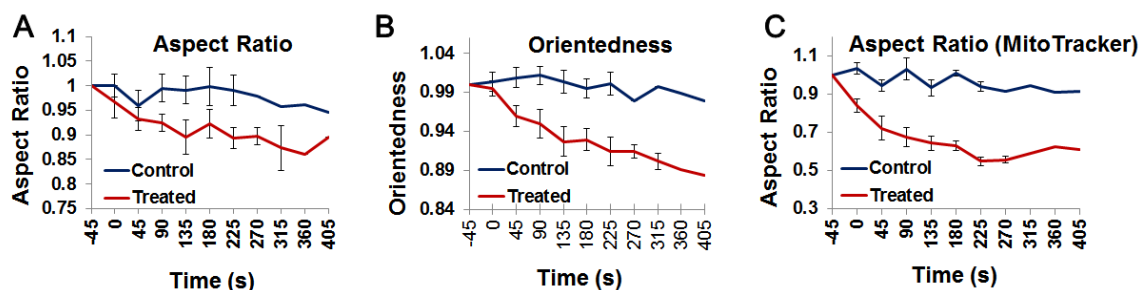


Figure 3-10 Segmented subcellular objects become rounder after calcium overload, as indicated by the aspect-ratio (A) and Orientedness (B). The decrease in the aspect ratio of objects within the fluorescence images (C) suggests that the change in the aspect ratio of mitochondria partially accounts for the decrease in the masked subcellular objects' aspect ratio. The data show mean and standard error for $n=6$ cells for the first 6 timepoints (treated) and the first 7 timepoints (control). Additional timepoints were tested for one control cell and 4 of the treated cells.

3.3.5 Texture-features can detect subcellular morphological dynamics induced by injury

Calcium-injury perturbs the spatial arrangement of the subcellular organelles. Such rearrangement is a result of changes in organelle morphology, as well as cell-shrinkage. While the treatment produces objects with a decreased aspect ratio and orientedness (Figure 3-10), relative distances among organelles also change and reduce as the cell shrinks. To quantify these two-dimensional, cell-wide, structural changes associated with the injury, we analyzed the texture of the masked Orientedness images as a function of time. To this end, we extracted 8 texture-features²¹⁻²³ using the code available²⁴ to analyze the spatial variation in the Orientedness values. As proposed in Ref. 23, we grouped the features into three categories; features that describe the smoothness

(Contrast, Dissimilarity and Inverse Difference Moment (IDM) or Homogeneity), uniformity (Entropy, Maximum Probability and Energy) and correlation (Autocorrelation, correlation) of the texture.

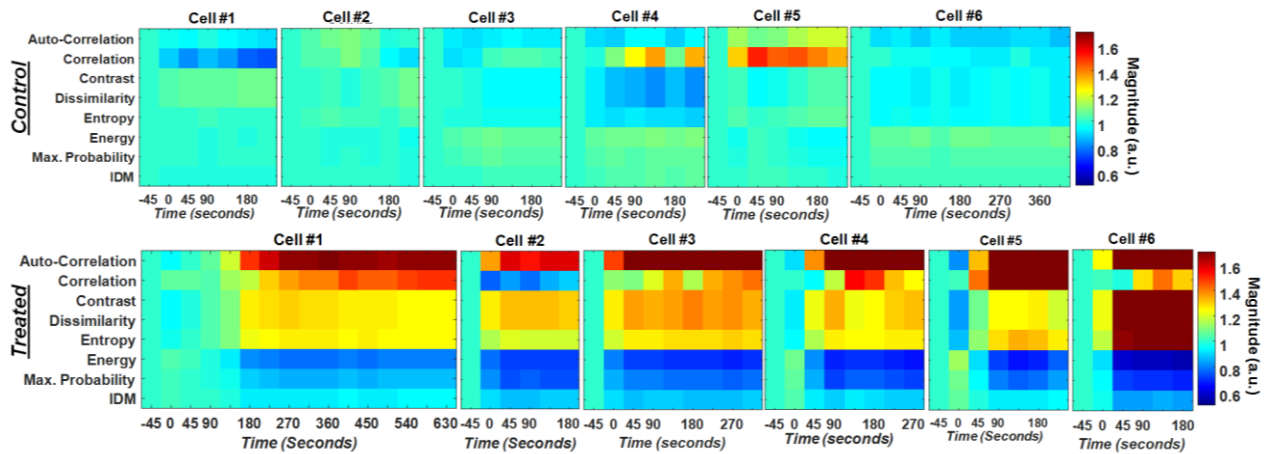


Figure 3-11 Changes in the texture-features of the masked orientedness images shown as heat-maps. Each row is a feature while each column is a time-point. Cells were monitored for different time periods, but for at least 180 seconds, after ionomycin treatment ($t=0$, Treated), or the same saline solution but with no ionomycin ($t=0$, Control). Texture-features are sensitive to the change in the spatial arrangement of the morphometric parameter Orientedness. The colorscale represents the magnitude of each parameter.

We found that multiple texture-features are sensitive to the morphological changes encoded by the orientedness images. We plotted these texture-features as a heat-map (Figure 3-11) for each cell, and observed the change in color over time, which indicates the features' ability to detect the underlying structural changes. Several features changed by more than 30% in the treated cells. Autocorrelation, Contrast, Dissimilarity and

Entropy increased in the treated cells, while they decreased slightly, or remained within 10% of the starting value in the control cells. Energy and Maximum Probability decreased in the treated cells, but remained within 10% of the starting value in the control cells. Cell-to-cell variations are also observed in both the control and treated cells. We also observed individual feature-responses for the whole dataset (Figure 3-12). Autocorrelation, correlation, Contrast, Dissimilarity and Entropy increase while Energy, Maximum Probability and IDM decrease over time in the treated cells compared with the control. We select Autocorrelation, Contrast, Entropy as the representative features from each group with positive trends (i.e. increase) and Energy and IDM as negative trends (i.e. decrease). We then calculate the composite feature by subtracting the decreasing features from the increasing ones. The square root of the Energy feature is taken to match the unit with that of other features. The composite feature in Figure 3-13 also shows a shift from the baseline after injury.

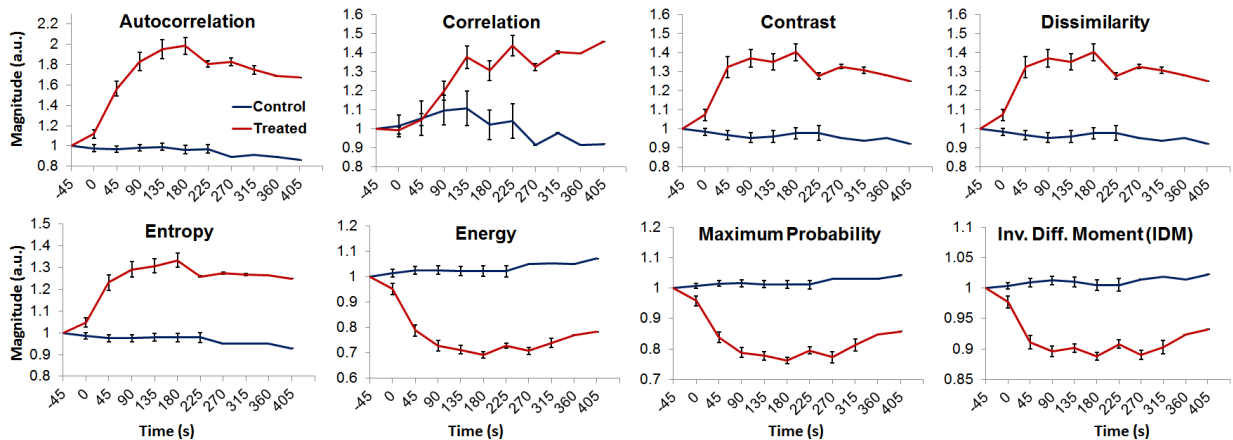


Figure 3-12 Average responses of the individual texture features over time. The smoothness of the texture decreases as the Contrast and Dissimilarity increase and IDM (also known as homogeneity) decreases in the treated cells compared with controls. The

uniformity of the texture decreases as the Entropy increases whereas the Energy and Max. Probability decrease. Correlation between pixels increases. The data show mean \pm standard error for timepoints at which more than one cell was tested.

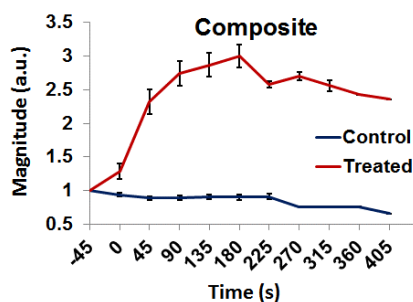


Figure 3-13 Composite feature calculated from representative features: Autocorrelation, Contrast, Entropy, Energy and IDM. The data show mean \pm standard error for timepoints at which more than one cell was tested.

3.4 Discussion

Cells and their subcellular organelles undergo morphological changes constantly. These changes occur either naturally or upon treatment. To quantify such morphological changes in an unstained cell, we utilized OSI to detect the scatterers present within the cell. However, tracking these scatterers and quantifying their morphology over time is a challenge since they are constantly shifting in space and changing shape. To address this problem, we present an algorithm to process angular-scatter- encoded images to detect as well as to track structural changes in the subcellular domain. With this algorithm, we generate a set of masks which are used to segment individual subcellular scatterers, and dynamically change shape in response to the morphological changes in the scatterers over time (Figure 3-5, Figure 3-6). These masks further allow us to extract morphometric

parameters, such as the aspect ratio of the segmented objects (Figure 3-10), or analyze the textural features of the mask-images (Figure 3-11, Figure 3-13).

To test this algorithm, we induced morphological changes by overloading endothelial cells with calcium. Excess calcium leads to the opening of the mitochondrial permeability transition (mPT) pores. Subsequent redistribution of small molecules and water causes swelling in the mitochondria²⁵. Due to calcium overload, a long mitochondrion may either remodel or undergo fission. Mitochondria undergoing remodeling become round whereas fission produces smaller fragments²⁶. With a sufficiently high calcium dose as used here, cells will also shrink and undergo cell death. As a result of this treatment, the organelles' morphology changes, as well as their subcellular structural arrangement, as the cell starts to shrink and subsequently die. This calcium treatment is similar to the one published in Ref .11. Thus, one significant aspect of this treatment is that it results in mitochondrial fragmentation and rounding. As we had previously observed, mitochondria in this study also attain a smaller and rounder shape post-injury as opposed to the elongated shape pre-treatment (Figure 3-8). Given the two-fold transformation in the morphology and arrangement of subcellular organelles upon treatment, we apply our algorithm and dynamic masks to track the scatterers over time and quantify their morphological changes. Our results show that the aspect-ratio and orientedness of the segmented objects in the masks decreases (Figure 3-10A and Figure 3-10B). This suggests that these masks are sensitive to the rounding of the organelles. This change was concurrent with a decrease in the aspect ratio of MitoTracker-labeled mitochondria (Figure 3-10C) suggesting that the decrease in the scattering objects' aspect ratio may be

at least partially accounted for by the rounding of the mitochondria becoming shorter and rounder upon calcium overloading.

We had used the “Orientedness” parameter previously to measure mitochondrial fission¹⁴. In that work, average Orientedness values were calculated for each cell, based on raw optical filtered intensities. The Orientedness parameter takes advantage of the fact that objects of different geometries (e.g. non-circular vs circular) have different directional light-scattering profiles. For example, light scattered from an elongated object is confined in a smaller azimuth angle, φ in the scatter-plane as compared to that of a round object¹¹. Orientedness measures this anisotropy of scattered light by taking the ratio of light-scatter signal at the direction of maximum scatter to the mean signal collected at all available directions¹⁴. This ratio is measured at each pixel, resulting in a cell-wide orientation mapping. However, since Orientedness is a normalized ratio of two intensity values, it is independent of signal strength at a given pixel, and pixels in the background may show orientation which doesn’t have any biological relevance. Hence, to amplify signal from the subcellular organelles as well as to suppress signal from background we present a modification of the Orientedness parameter that uses local energy information, instead of only raw intensity values. Local energy emphasizes regions of abrupt change in intensity such as edges in an image. We take this property of local energy to enhance the edges of the organelles as well as to suppress signal from monotonically varying intensity such as the background. By multiplying the Orientedness images with the masks we further extract signal from the major scattering sources, allowing us to analyze individual subcellular scatterers over time, as opposed to taking the average Orientedness across the whole cell. When tracked over time, we observe a

decrease in the Orientedness of the objects of the masks. While the aspect-ratio measures an object's shape directly by taking the ratio of the height and weight, Orientedness provides an indirect means to obtain similar information from the scattering profile of the object in question. As expected, when tracked over time, both of these parameters show a similar decreasing trend with time (Figure 3-6A and Figure 3-6B), indicating concordance between two approaches. Correlation between the fluorescent data (Figure 3-6C), and data obtained from the label-free approach, suggests that the morphological change probed by our optical scatter technique is pertinent to mitochondria. These results corroborate our previous data showing detection of mitochondrial rounding and fission with optical scattering^{11,14}. However, the present data improves on our previous parameters. Here, we generate a dynamic mask that can change shape over time to extract Orientedness values only from the scatterers within the cell and discard background pixels. Thus, our current data are less sensitive to background and can enable tracking of individual scatterers.

To generate our subcellular organelle masks, we apply a segmentation technique originally proposed for digital Gabor-filtered images¹⁶, and multiply the resulting segmentation mask with the Orientedness image. The masked-Orientedness images therefore contain orientation information from significant scatterers in the cell. As the organelles change shape, the transformation of their Orientedness values will impact the spatial relationship between two pixels. In addition, the spatial arrangement of the organelles will also be affected by the shrinkage of the cell upon injury. While the change in the individual masked objects reflects changes in individual structures, the spatial distribution and arrangement of these structures may be quantified using various image-

based texture-features. Our texture analysis shows that Autocorrelation, correlation, Contrast, Dissimilarity and Entropy increase while Energy, Maximum Probability and IDM decrease over time (Figure 3-12). However, as suggested by Haralick, even though these features show sensitivity towards change in texture, it is difficult to identify which textural characteristic is signified by each of them²¹. Hence it will be hard to draw any biological relevance of the extracted features. Thus, one way to represent the underlying biological events is to combine these features and observe their ensemble behavior in one composite textural parameter (Figure 3-13). Taken together, our data allow for single-scatterer analysis via the analysis of the individual masked objects, and whole-cell analysis via the textural features. The textural features are indicative of an overall cellular dynamic morphological state that changes in response to treatment.

There are several other studies which have recently demonstrated the potential of label-free methods used in conjunction with computational image processing, for cellular analysis and classification. For example, Blasi et al. proposed a label-free approach to detect DNA content and quantify mitotic cell cycle phases by combining conventional flow cytometry and single-cell imaging³. The phases were classified using morphological features extracted from bright-field and dark-field images. In this paper, we use similar features such as aspect-ratio and Haralick textures. However, one major difference here, is the use of the Orientedness parameter which is based on light-scattering. Since light-scattering is directly related to the size and shape of the probed objects, the Orientedness parameter contains valuable information regarding morphological changes in the subcellular organelles.

One of the limitations of the technique presented here is its dependency on image-processing parameters that generate local energy and phase-congruency images. However, once these parameters are tuned empirically for a specific cell type, they are constant for any number of samples. This procedure will be automated in the future. The proposed features can also be used in conjunction with other dynamic parameters such as velocity and displacement of the organelles in biologically relevant cases such as mitochondrial mobility, fission/fusion rate etc. The combined approach can then be used to provide a better label-free quantification of subcellular dynamics.

In conclusion, we have developed a label-free approach to detect and track subcellular morphological changes dynamically. This technique does not use any exogenous marker and hence can be used to avoid the adverse effects of label-based assays and potentially provide a method for rapid drug-screening. In the future, we hope to apply this technique to different mammalian cell types such as neurons, to quantify subcellular dynamics upon chemically and mechanically induced injuries.

Acknowledgements

This paper is based in part on the SPIE proceedings paper titled “[*Label-free Fourier filtered dark-field imaging to quantify subcellular dynamics*](#)”, [by Mohammad Naser, Rene S. Schloss and Nada N. Boustany](#), Proc. SPIE 10504, Biophysics, Biology and Biophotonics III: the Crossroads, [Adam Wax](#); [Vadim Backman](#), Editor(s), 105040G (20 February 2018); doi: [10.1117/12.2290908](#). This work was partially supported by Grant CBIR14PIL005 from the New Jersey Commission on Brain Injury Research and NSF grant CBET[1512170](#). We thank Dr. Mathieu Petitjean of Pharmanest, LLC (Princeton, NJ) for insightful discussions regarding the analysis of the masked subcellular objects.

Appendix

Table 3-1 Expression for Gabor filters in frequency domain

General expression of a Gaussian function: $H(u, v) = A * e^{\left[\frac{-(u-U)^2+(v-V)^2}{2\sigma_{frequency}^2} \right]}$; $\sigma_{frequency} = \frac{1}{2\pi\sigma_{space}}$; with

$$\sigma_{space} = \frac{S}{2}.$$

Hence, $\sigma_{frequency} = \frac{1}{\pi S}$

Replacing $\sigma_{frequency}$ in the general expression, we obtain:

$$H(u, v) = A * e^{\left[\frac{-(u-U)^2+(v-V)^2}{\pi^2 S^2} \right]}, \text{ Where, Period, } S = \frac{1}{F} = \frac{1}{\sqrt{U^2+V^2}}$$

$$H(u, v) = A * e^{-\frac{\pi^2}{2*(U^2+V^2)}[(u-U)^2+(v-V)^2]}$$

References

1. R. Dixit et al., "Cell damage and reactive oxygen species production induced by fluorescence microscopy: effect on mitosis and guidelines for non-invasive fluorescence microscopy," *Plant J.* **36**(2) 280-290 (2003).
2. J. F. Buckman et al., "MitoTracker labeling in primary neuronal and astrocytic cultures: influence of mitochondrial membrane potential and oxidants," *J. Neurosci. Methods* **104**(2) 165-176 (2001).
3. T. Blasi et al., "Label-free cell cycle analysis for high-throughput imaging flow cytometry," *Nat. Commun.* **7**, 10256 (2016).
4. M. C. Skala et al., "In vivo multiphoton microscopy of NADH and FAD redox states, fluorescence lifetimes, and cellular morphology in precancerous epithelia," *Proc. Natl. Acad. Sci.* **104**(49), 19494-19499 (2007).
5. C. Mujat et al., "Endogenous optical biomarkers of normal and human papillomavirus immortalized epithelial cells," *Int. J. Cancer* **122**(2) 363-371 (2008).
6. N. N. Boustany et al., "Microscopic imaging and spectroscopy with scattered light," *Annu. Rev. Biomed. Eng.* **12**, 285-314 (2010).
7. L.T. Perelman et al., "Observation of periodic fine structure in reflectance from biological tissue: a new technique for measuring nuclear size distribution," *Phys. Rev. Lett.* **80**(3), 627-630 (1998)
8. A. Wax et al., "Cellular organization and substructure measured using angle-resolved low-coherence interferometry," *Biophys. J.* **82**(4), 2256-2264 (2002).

9. J. D. Wilson et al., "Light scattering from intact cells reports oxidative-stress-induced mitochondrial swelling," *Biophys. J.* **88**(4), 2929-2938 (2005).
10. X. T. Su et al., "Light scattering characterization of mitochondrial aggregation in single cells," *Opt. Express* **17**(16) 13381-13388 (2009).
11. N. N. Boustany et al., "Calcium-induced alterations in mitochondrial morphology quantified in situ with optical scatter imaging," *Biophys. J.* **83**(3), 1691-1700 (2002).
12. N. N. Boustany et al., "BCL-xL-dependent light scattering by apoptotic cells," *Biophys. J.* 0006-3495 **87**, 4163-4171 (2004).
13. H. Sierra et al., "Measurement of object structure from size-encoded images generated by optically-implemented Gabor filters," *Opt. Express* **20**(27), 28698-28706 (2012).
14. R. M. Pasternack et al., "Detection of mitochondrial fission with orientation-dependent optical Fourier filters," *Cytometry A* **79**(2), 137-148 (2011).
15. P. Kovesei et al., "Image features from phase congruency," *Videre: J. Comput. Vis. Res.* **1**(3), 1-26 (1999).
16. A. K. Jain et al., "Unsupervised texture segmentation using Gabor filters," *Patt. Rec.* **24**(12), 1167-1186 (1991).
17. J. W. Goodman, *Introduction to Fourier optics*, 3rd ed, Roberts and Company Publishers (2005).
18. P. Kovesei, "MATLAB and Octave functions for computer vision and image processing," Online: <http://www.peterkovesei.com/matlabfns/PhaseCongruency/phasecong3.m> (accessed March 07, 2018).
19. F. W. Campbell et al., "Application of Fourier analysis to the visibility of gratings," *J. Physiol.* **197**(3), 551-566 (1968).
20. R. C. Gonzalez and R. E. Woods, *Digital image processing*, 2nd ed., Prentice Hall, ch9, (2007).
21. R. M. Haralick et al., "Textural Features of Image Classification," *IEEE T. Syst. Man Cyb.* **SMC-3**(6), 610-621 (1973).
22. L. K. Soh et al., "Texture Analysis of SAR Sea Ice Imagery Using Gray Level Co-Occurrence Matrices," *IEEE T. on Geosci. and Remote Sensing* **37**(2), 780-795 (1999).
23. D. A. Clausi, "An analysis of co-occurrence texture statistics as a function of grey level quantization," *Can. J. Remote Sensing* **28**(1), 45-62 (2002).
24. <https://www.mathworks.com/matlabcentral/fileexchange/55034-glcmmfeatures-glcmm>
25. R. Jemmerson et al., "Cytochrome C release from CNS mitochondria and potential for clinical intervention in apoptosis-mediated CNS diseases," *Antioxid. Redox Signal.* **7**(9-10), 1158-1172 (2005).
26. S. Deheshi et al., "Changes in mitochondrial morphology induced by calcium or rotenone in primary astrocytes occur predominantly through ros-mediated remodeling," *J. of Neurochem.* **133**(5), 684-699 (2015).
27. Q. Zhao et al., "Phosphorescent heavy-metal complexes for bioimaging," *Chem. Soc. Rev.* **40**(5) 2508-2524 (2011).
28. Z. Zhang et al., "Quality control of cell-based high-throughput drug screening," *Acta Pharm. Sin. B* **2**(5) 429-438 (2012).

CHAPTER 4

4 LIGHT SCATTER BASED LABEL-FREE ASSESSMENT OF GLUTAMATE INDUCED EXCITOTOXICITY ON MITOCHONDRIAL DYNAMICS

Abstract

Abnormal mitochondrial morphology and dysfunction have been associated with diseases such as Alzheimer's, Parkinson's, Amyotrophic lateral sclerosis (ALS) as well as Traumatic Brain Injury (TBI)¹⁻³. Such discoveries have motivated researchers toward the development of mitochondria-targeted therapy⁴. This in turn necessitates an accurate assessment of mitochondrial dynamics. Traditional mitochondria targeted dyes or mitochondria-targeted fluorescent proteins affect mitochondrial metabolism⁵ and dynamics⁶ adversely. In this chapter, we investigate how we can quantify mitochondrial dynamics in neurons without the use of fluorescent dyes. For this purpose we applied a modified version of our previously reported label-free parameter S_{\max} ²⁰. We found that S_{\max} is more appropriate for neurons than the Orientedness parameter used for BAEC cell in the previous chapter. We will use glutamate to induce injury of dissociated neurons and investigate mitochondrial dysfunction. This chemical injury mimics the cellular events that take place in neurons during traumatic brain injury (TBI) Administering lethal doses of Glutamate induces TBI-like mitochondrial dysfunction via calcium-overload⁷⁻⁹. Our goal is to assess the severity of the chemical insult on mitochondrial morphology and function using the label-free light-scatter based technique. This technique doesn't use any exogenous marker and hence can be used to develop alternatives to the label-based assays

and potentially provide a method for rapid drug-screening. Techniques developed in this project can ultimately help to develop and test mitochondria-targeted neuroprotective therapies.

4.1 Introduction

Mitochondrial structure determines function. It has been reported that alterations in mitochondrial morphology is an early event in several neurodegenerative diseases. There's a growing interest toward identifying alterations in mitochondrial structure in pathological conditions. Perkins *et al.* provided a catalogue of mitochondrial structural alterations from various neurodegenerative diseases¹⁰. These changes mainly involve membrane rupture, cristae disorganization, matrix swelling, vacuolation, alteration in overall shape and size etc. Another way to look at morphology-change is to assess mitochondrial dynamics such as fission and fusion processes. In healthy state, mitochondrial morphology is regulated by the balance between these two processes; however, there is substantial evidence that the balance is compromised in neurodegenerative diseases¹¹. Altogether, any abnormality in mitochondrial structure affects its normal functions which ultimately lead to pathological conditions.

In traumatic brain injury (TBI), similar ultra-structural alterations as well as imbalance in fission-fusion activities are reported. Primary force in TBI causes excessive release of excitatory neurotransmitter such as glutamate. In the secondary stage, this leads to a high level of intracellular and mitochondrial Ca^{2+} accumulation. Overloading of Ca^{2+} causes alterations in mitochondrial morphology⁹ and imbalance between fusion and fission rate¹². It also affects organelle trafficking⁷. These events lead to overproduction of catabolic free radicals that activates cell-death signaling pathways¹³. The structural

changes observed in TBI include swollen mitochondria, disruption of the cristae and rupture of outer membrane¹⁴. Detailed molecular mechanism of mitochondria-mediated cell death is described by Walker *et al*¹⁵.

4.1.1 Role of glutamate

Increased glutamate initiates the process of intracellular calcium overload¹⁵. Ionotropic glutamate-receptors such as N-methyl-D-aspartate receptor (NMDAR), 2-amino-3-(3-hydroxy-5-methylisoxazol-4-yl) propionate receptor (AMPA) and kainate receptor subtypes are activated upon the binding of glutamate. Normal activation of these receptors allows Na⁺, K⁺ and Ca²⁺ to permeate through corresponding receptor-operated channels (ROCs). However, overactivation of these receptors causes excitotoxicity in TBI which leads to cell-death¹⁵.

4.1.2 Role of calcium

The “Calcium hypothesis” for TBI postulates that the excessive presence of Ca²⁺ is the cause of excitotoxicity in neurons¹⁶. Elevated Ca²⁺ activates Ca²⁺-dependent enzymes and overloads the mitochondria¹⁷ initiating a cascade of events which leads to either rapid necrotic or delayed cell-death (apoptosis). It is shown that calcium overload causes opening of mitochondrial permeability transition (mPT) pores⁹ which is identified as the onset of structural alterations using electron micrographs¹⁴. Osmotic swelling due to mPT causes loss of cristae organization and rupture of the outer membranes.

4.1.3 Assessment of mitochondrial dynamics via imaging techniques

For this project, we intend to develop an optical technique that can assess mitochondrial morphology and/or dynamics in normal and injured neurons. Next, we will compare the non-invasive label-free approach with the traditional approaches mentioned below.

4.1.3.1 Traditional approach

Fluorescent dyes or mitochondria targeted fluorescent proteins have been used to track mitochondrial dynamics. Fluorescent labeling provides localization, specificity, and better contrast; however, it has some adverse effects. MitoTracker dyes reduce cell motility in primary neuronal culture as well as alter their morphology⁶. Besides, some dyes are not photo-stable if used in low concentration to avoid quenching effect, whereas fluorophores tend to aggregate and stain other organelles if used in high concentration¹⁸. On the other hand, mitochondria targeted fluorescent proteins such as mito-GFP do not affect function or morphology; however, long-duration time-lapse imaging is not possible due to photo-toxicity⁵. Moreover, low transfection efficiency hinders High Throughput Screening (HTS) for drug discovery¹⁹. Hence a label-free imaging technique would be ideal for fast and noninvasive quantification of the mitochondrial dynamics over a long period.

4.1.3.2 Label-free Optical Scatter Imaging

To quantify mitochondrial morphology we had used Orientedness for BAEC cells in Chapter 3, however since the edges of the neuronal processes are already oriented in a given direction, the Orientedness value is higher on the processes in comparison to the internal organelles (Figure 4-1). Hence, even though the organelles inside the processes undergo morphological changes, it is not truly reported by the Orientedness parameter.

Therefore, we resort to a parameter called S_{\max} , developed previously by our laboratory²⁰. S_{\max} is the value of the Gabor filter-period which responds maximally to a probed object. For each pixel in an image, the S_{\max} value is generated. Thus a spatial mapping of the size of the objects probed by the Gabor-filters can be obtained. For this work, we have added the filter-responses from all 8 orientations first and then the filter-period producing the maximum response was identified. In addition, the S_{\max} image is masked by applying the image segmentation method described in Chapter 3 to discard data from no-cell region.

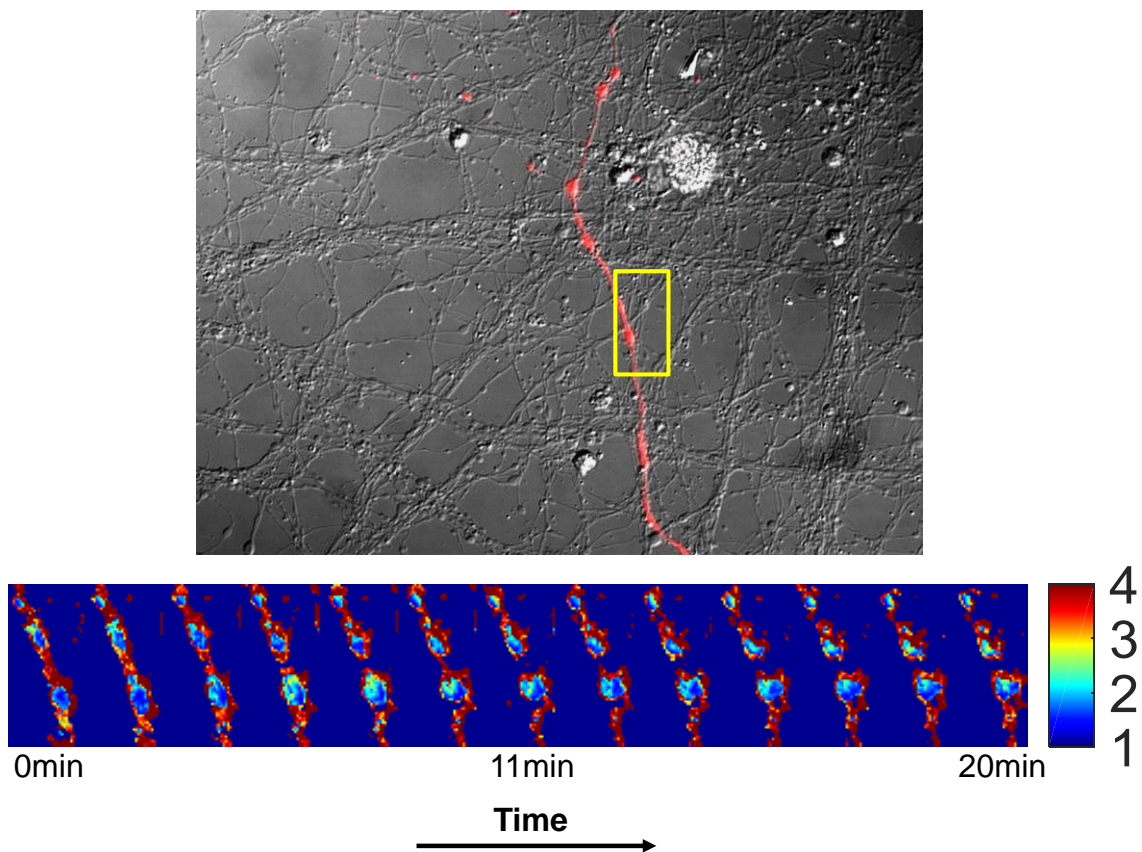


Figure 4-1 Evolution of orientedness in neuronal processes. (top) mCherry transfected mitochondria located in neuronal processes in DIC image (bottom) Orientedness image of the ROI with yellow border. Note the highly oriented edges of the

processes compared to the intracellular mitochondria. Colorbar indicates Orientedness values (a.u.). The sample is treated with 120 μ M glutamate.

4.2 Methods

4.2.1 Cell culture and Transfection

Hippocampal neurons were collected from rat embryos on day 18 embryonic (E18) as previously described²¹. Cells were plated on poly-D-lysine (PDL) coated coverslips (Fisher Scientific) placed in 12-well plates (Sigma). Coverslips were coated with 10 μ g/mL PDL (Sigma) overnight at 4°C covered in foil. Wells containing coverslips were then washed with sterile water and dried for 1 hour before plating. Cells were plated at a density of ~50,000 cells per well. Cultures were maintained in neuro-basal media supplemented with 2% B27, 1% GlutaMAX in a 37°C incubator with 5% CO₂. Neurons were transfected with mCherry-Mito-7 (Addgene plasmid # 55102) on DIV6. For the 12 well plate, the transfection media was prepared by mixing 18 μ g DNA and 18 μ L PLUS reagent in 2.4mL Opti-MEM (reduced serum media) first. Then 24 μ L of Lipofectamine (ThermoFisher) was added as the transfection reagent. The transfection mix was added dropwise in each well after the conditioned medium in which the neurons were being cultured was saved and replaced by new neuro-basal media where the ratio of transfection mix and neuro-basal media was 1:4. The cells were then incubated for 60min in 37°C. Afterwards, the incubation media was replaced by the conditioned media and left in 37°C until imaging on DIV12-16. For fluorescence labeling with Mitotracker, cells were incubated in HEPES Buffered balanced Salt Solution (HBSS) medium supplemented with 100nM Mitotracker Green for 45min. HEPES Buffered balanced Salt Solution can be prepared with 1.802mM CaCl₂, 0.8119mM MgCl₂, 0.9058mM

$\text{NaH}_2\text{PO}_4 \cdot \text{H}_2\text{O}$, 51.3347mM NaCl, 5.3654mM KCl, 24.97mM D-glucose, 26.188mM NaHCO_3 , and 10.9105mM HEPES.

4.2.2 Glutamate treatment

Cells were treated with 120 μM Glutamate, dissolved in HEPES Buffered Balanced Salt Solution (HBBSS) and 10 μM Glycine. The coverslip was mounted on a steel plate and the fluid was flushed inside the chamber between the coverslip and plate, as described in the previous chapter.

4.2.3 Image acquisition

Gabor-filtered images were acquired using the same gabor filters described in chapter 3.

4.2.4 Image processing

Acquired Gabor-filtered data is pre-processed first by background subtraction and standardization. Background subtraction is performed by morphological opening operation. The data from all filter images is standardized by subtracting the mean and dividing by the standard deviation to obtain zero mean and unit variance. The processed data is then fed to a k-means classifier for segmentation. The classifier assigns all pixels to 4 different classes based on the scattering intensity and each pixel-location is assigned a class- number. The output of the classifier is reshaped into a 2D image where pixels belonging to a class are pseudo-colored in same color, thus generating a segmented image similar to Figure 3-4. However, note that no phase-congruency is used in the pre-processing step before classification to generate this image. We call this pseudo-colored image a Segmented image. Each of the colors indicates a class of pixels that contain objects scattering with similar intensity. Specifically, the no-cell region has the minimal intensity and can be discarded. For this work, we consider the pixels that correspond to

the neuronal processes, subcellular organelles etc. By keeping the corresponding classes, we create a binary image which will be used to extract information from size-encoded “ S_{\max} ” image described below. We refer to this binary image as Mask image.

To generate the S_{\max} image, first, filter-responses from all orientations for a specific period (S) are added. This results in 6 images for 6 periods. Then the filter-period with the maximum intensity at each pixel is found. Each pixel is then assigned the period value and pseudo-colored to obtain a S_{\max} image. The S_{\max} image is then multiplied by the Segmented image to extract size information only from the neuronal processes and subcellular organelles.

4.3 Results

4.3.1 Reporting change in organelle-size

Mitochondria and other organelles which are dynamic, constantly change their shape. This change in shape and size is visible in the pseudo-colored S_{\max} image (Figure 4-2). Each pixel in the S_{\max} image represents the size of the object located in that pixel. The S_{\max} images are masked using the Segmented images. However, all clusters except the background are added together to create the mask for neurons. The dark-field and corresponding S_{\max} images in Figure 4-2 show five different representative time-points of an organelle changing its shape. The change in morphology is quantified using the histogram of the S_{\max} values where the distribution of sizes varies with the change in shape. To observe an overall change in size, the mode or the most occurring S_{\max} value in the region of interest (ROI) is taken and plotted over time (Figure 4-3). A ‘big’ organelle probed by $2\mu\text{m}$ filter-period is labeled in dark-blue at time 0min whereas ‘smaller’ fragments of that organelle probed by $1.43\mu\text{m}$ filter-period are labeled in lighter

blue at the next time-point (Figure 4-2). The ‘jumps’ at 1.20min and 17min compared to the previous time-points in the Smax and histograms (Figure 4-3) are also noticeable in the mode plot.

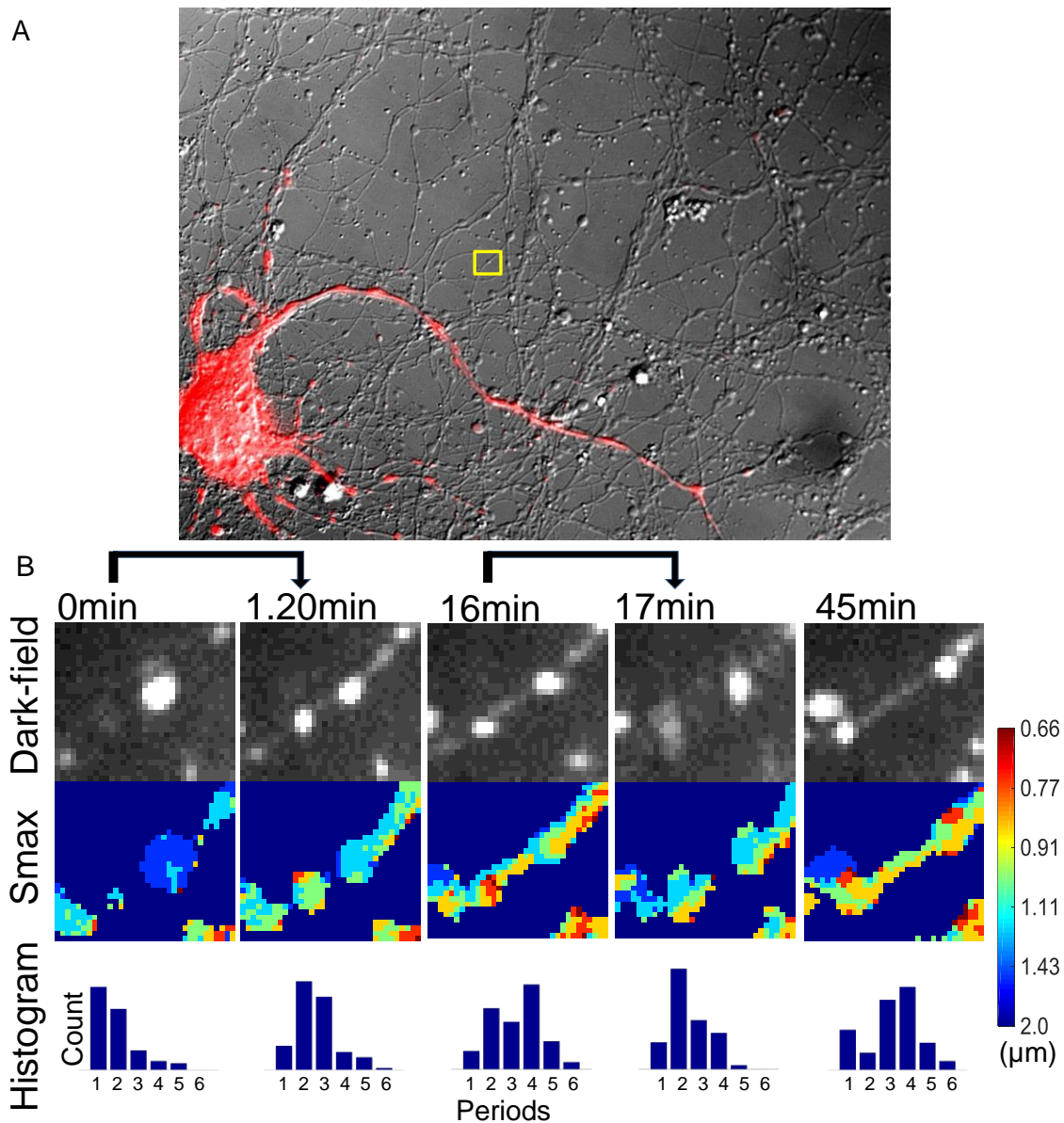


Figure 4-2 Tracking change in organelle-shape in an un-transfected neuronal process (yellow ROI). (A) mCherry transfected mitochondria located in neuronal processes in DIC image (B-top) Dark-field images showing time-lapse images of an organelle

changing its shape.(B-middle) corresponding S_{\max} images indicating difference in size and (B-bottom) histogram showing the distribution of sizes, i.e. S_{\max} values. The sample was treated with 120 μ M glutamate.

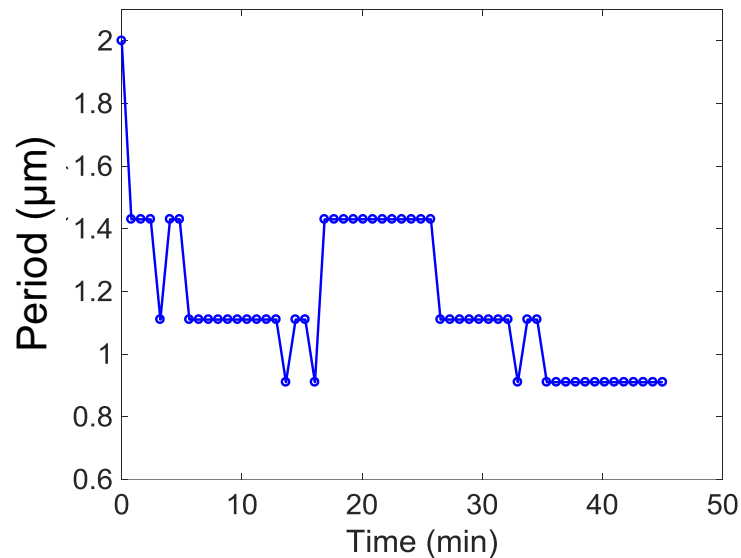


Figure 4-3 Most frequent S_{\max} value in the ROI over time may be used to track the morphological changes in the images object.

4.3.2 Tracking organelle movement

The movement of the organelles can also be tracked from the Segmented image using a kymograph. The Kymograph plugin available for ImageJ (Fiji) is used to track the spatial movement of organelles over time. Also, to demonstrate that the proposed label-free technique can track organelles irrespective of labeling, we compare two cases where the organelle is not labeled in one (Figure 4-4) and labeled with mitochondria specific MitoTracker dye (Figure 4-5) in the other. Different time points are annotated on the Kymographs for comparison with the organelle-location in the Segmented image. While in Figure 4-4 it cannot be ascertained that the organelle in the ROI is mitochondria, in

Figure 4-5 the presence of mitochondria is indicated by the fluorescence. A kymograph obtained using the time-lapse fluorescent images are also shown along the label-free kymograph in Figure 4-5 for the mitochondria. Note in the time-lapse Segmented images

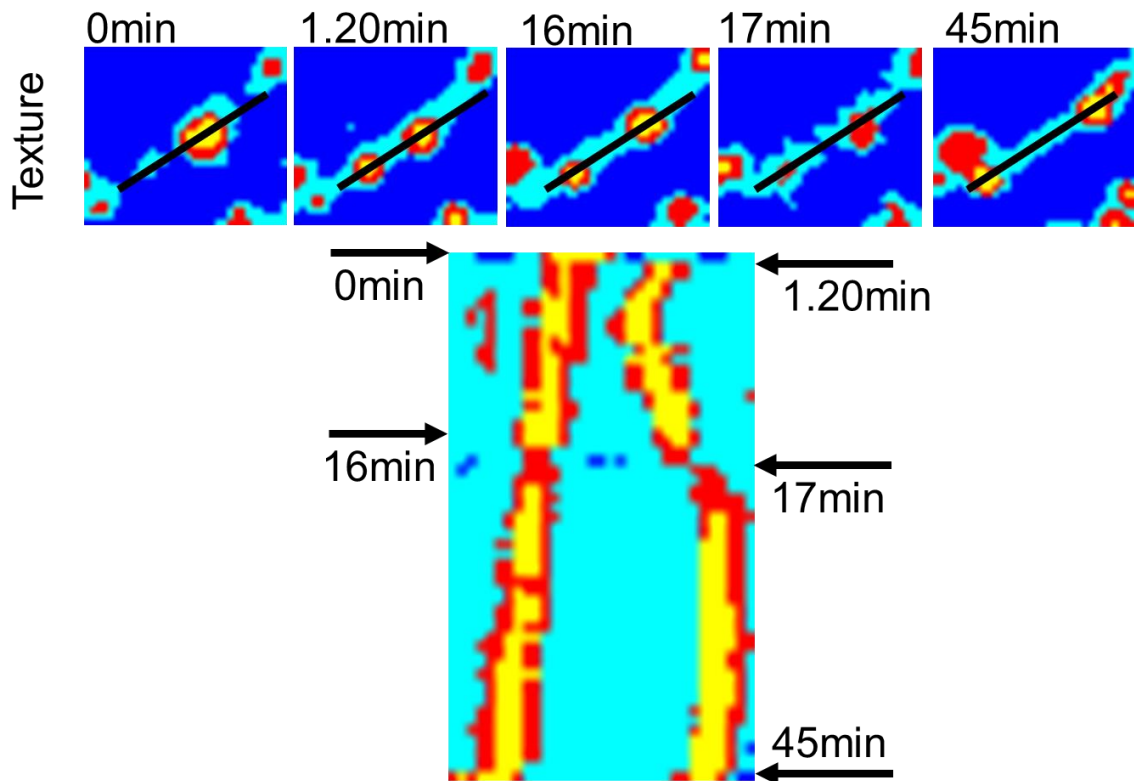


Figure 4-4 Kymograph showing organelle spatial movement over time (same ROI of Figure 4-2 A). (top) Time-lapse Segmented images; black line indicates the probe for kymograph, (bottom) Kymograph along the black lines on the labeled images over time. Organelle fission at 1.20min can be noticed along with displacement over time. The sample was treated with $120\mu\text{M}$ glutamate.

and corresponding kymograph that after the mitochondrial fission at 2.48min the bottom mitochondrion moves down while the top part remains immobile. Interestingly, the top part is missing in the fluorescent images, even though it is visible in the Segmented and

the dark-field images. We cannot say for sure why the top mitochondrion stopped fluorescing, but the label-free Segmented image and the kymograph can still track it till the end of the observation period. In addition, the label-free kymograph is impervious to photo-bleaching when compared with the fluorescent kymograph. As can be seen in the fluorescent time-lapse images, the mitochondrion in the last time-point is vaguely visible, but the label-free kymograph can still track the mitochondrion.

4.4 Discussion

In terms of morphology, neurons as cell are starkly different from the Bovine Aortic Endothelial Cells (BAEC) used in the previous chapter; for instance, neurons have processes which spread like a network in a given culture. Such morphology calls for a modification of the label-free parameter through which changes in morphology will be quantified. Since the edges of the processes give high Orientedness value (Figure 4-1), the Orientedness parameter might be misleading while assessing the change in orientation of the organelles inside the processes. Our previously reported label-free parameter S_{\max} ²⁰ can indirectly track the change in size. S_{\max} maps the organelle size instead of its orientation. And since S_{\max} is a spatial map of the cell, the shape of the organelles can be visually observed and possibly quantified. However, in this chapter we have focused only on the change in size and movement of the organelle. We have shown that the S_{\max} is capable of reporting changes in organelle morphology in Figure 4-2 and Figure 4-3. The varying distribution of sizes in Figure 4-2 is indicative of the presence of objects of different sizes within the organelles or in the processes as the organelle are morphing into various shapes and moving through the processes.

Another aspect of mitochondrial assessment in neurons is their movement. It has been shown that Glutamate induced injury mimicking TBI slows mitochondrial motility⁷.

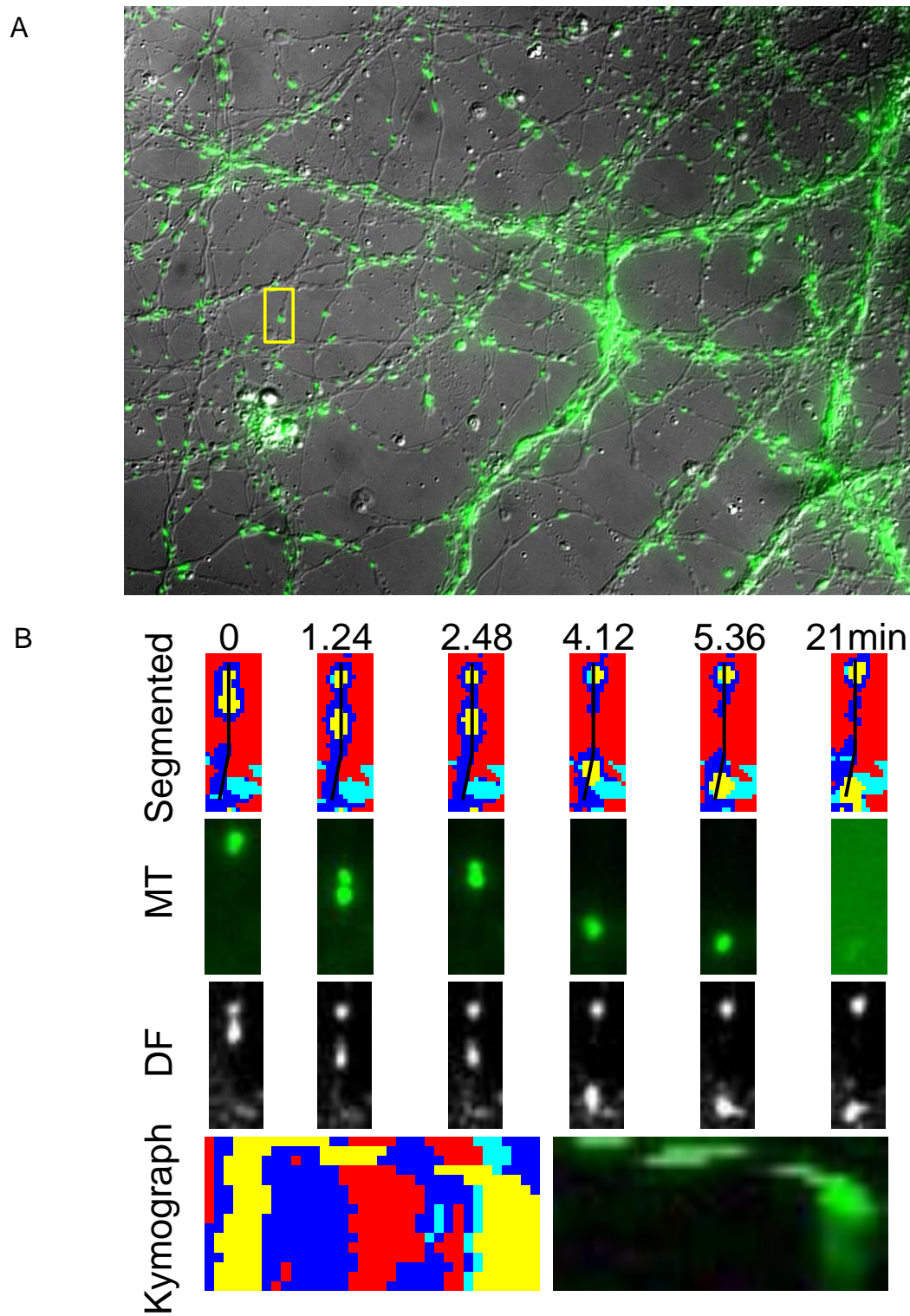


Figure 4-5 Comparing kymographs generated from label-free Segmented and MitoTracker labeled fluorescent images. (top) time-lapse Segmented image (mid) time-

lapse MitoTracker (MT) fluorescent image and dark-field (DF) images (bottom) kymograph obtained from the Segmented images track both labeled and unlabeled mitochondria whereas the fluorescent kymograph tracks organelle as long as it is fluorescing or not bleached. This is a control sample with no glutamate treatment.

We have shown in Figure 4-4 and Figure 4-5 that organelle or mitochondrial movement can be tracked in the label-free Segmented images, even after the fluorescence bleaches out. Thus live-cell imaging can be possible for longer duration. Also several reports suggested fluorescent induced photo-toxicity⁵, which we plan to verify against our label-free technique in the future to demonstrate the compatibility of the approach for non-invasive imaging.

It should be mentioned here that the mode plot shown in Figure 4-3, can be affected by the size of the ROI. Here we have restricted the window only to the spatial location where an organelle is undergoing morphological changes and hence very little of the surrounding processes is included. Also, the mode of the S_{\max} histogram values would change if other processes are included in the ROI. A rule of thumb for ROI selection can be discarding the part of the processes that the organelle is not reaching or not undergoing any morphological change.

The ROI shown in Figure 4-2 and Figure 4-4 are from the glutamate treated neurons and the ROI in Figure 4-5 is from the control group. These images are the proof-of-concept images for label-free tracking of organelle morphology and movement respectively. Although we set out to probe morphological changes caused by glutamate treatment, further investigation is required to establish the proposed technique as a label-

free approach to detect the underlying biology. One of the challenges involved is the dominance of bigger objects which overshadows the smaller objects located inside them. For example, signal from the organelle is dominated by that of the processes. As can be seen in Figure 4-6, the S_{\max} values of the axonal region indicate the presence of bigger objects in blue color, as reported by the bigger periods. Here the signal from the axon is greater than that of mitochondria, and hence the corresponding pixels represent the axon instead of the mitochondria. However, this is only the case when the processes is bigger than the organelle inside of it. If, on the other hand, the organelle occupies most of the space inside of a processes and is bigger than the average width of processes, the signal from the organelle will dominate. In such cases, the morphological changes in the organelle can be reported better by the filters, as can be seen in Figure 4-2 and Figure 4-4. The organelle shown in those images are from ROI 2 of the DIC image in Figure 4-6. The processes that contains this organelle is thinner than the axon shown in ROI 1. Hence the signal from the organelle dominates which makes it visible in the S_{\max} image in Figure 4-2.

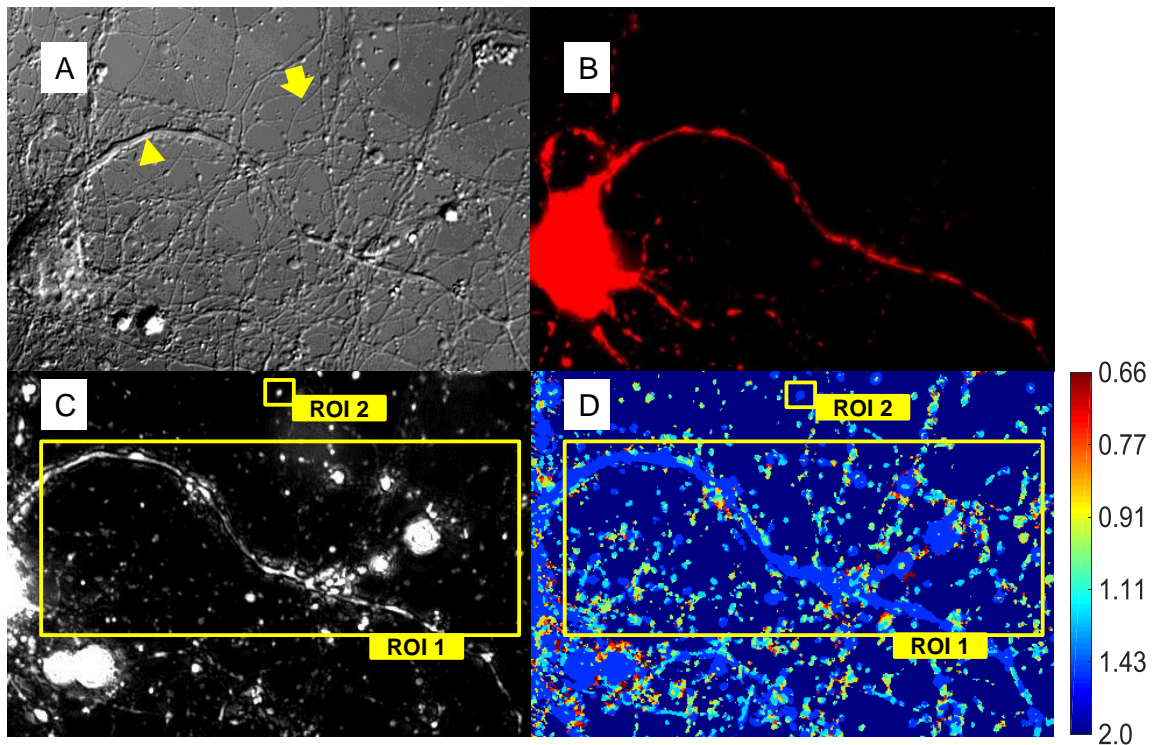


Figure 4-6 Signal from broader processes dominate S_{\max} image (A) DIC image showing a neuron with axon which is broader (arrow-head) than a thin processes (arrow) (B) mCherry transfected neuron shows location of mitochondria (C) dark-field image (D) S_{\max} image showing the S_{\max} values in two ROIs. The axon shown in the DIC image is probed by the biggest period and hence colored blue. The mitochondria, shown in red in the fluorescent image, are not visible in the S_{\max} image.

The applicability of this label-free approach to track morphology and movement of an organelle may make it useful for initial screening of any morphological change in a cell upon drug administration. Also, this technique can be used for repeated assessment of morphology once initial screening is conducted and the changes are related to the underlying biology. Thus time-consuming and difficult transfection procedures can be avoided.

In this chapter, we have presented a modified version of a previously reported label-free parameter which encodes size and have demonstrated that it can be used to probe the morphological changes in neurons. We have also shown an alternative to the fluorescent based kymograph generally used to record mitochondrial movement. However, more analysis is required to establish a method for differentiating between mitochondria and other mobile organelles. And more work is needed to find reproducible differences between treated and untreated neurons.

References

1. Petrozzi L, Ricci G, Giglioli NJ, Siciliano G, Mancuso M. Mitochondria and neurodegeneration. *Biosci Rep.* 2007 Jun;27(1-3):87-104. PubMed PMID: 17486441. Epub 2007/05/09.
2. Fukui H, Moraes CT. The mitochondrial impairment, oxidative stress and neurodegeneration connection: reality or just an attractive hypothesis? *Trends in neurosciences.* 2008;31(5):251-6.
3. Mattson MP, Gleichmann M, Cheng A. Mitochondria in neuroplasticity and neurological disorders. *Neuron.* 2008;60(5):748-66.
4. Wang W, Karamanlidis G, Tian R. Novel targets for mitochondrial medicine. *Science translational medicine.* 2016;8(326):326rv3-rv3.
5. Dixit R, Cyr R. Cell damage and reactive oxygen species production induced by fluorescence microscopy: effect on mitosis and guidelines for non-invasive fluorescence microscopy. *The Plant Journal.* 2003;36(2):280-90.
6. Buckman JF, Hernández H, Kress GJ, Votyakova TV, Pal S, Reynolds IJ. MitoTracker labeling in primary neuronal and astrocytic cultures: influence of mitochondrial membrane potential and oxidants. *Journal of neuroscience methods.* 2001;104(2):165-76.
7. Rintoul GL, Filiano AJ, Brocard JB, Kress GJ, Reynolds IJ. Glutamate decreases mitochondrial size and movement in primary forebrain neurons. *Journal of Neuroscience.* 2003;23(21):7881-8.
8. Dugan L, Sensi S, Canzoniero L, Handran S, Rothman S, Lin T-S, et al. Mitochondrial production of reactive oxygen species in cortical neurons following exposure to N-methyl-D-aspartate. *Journal of Neuroscience.* 1995;15(10):6377-88.
9. Dubinsky JM, Levi Y. Calcium-induced activation of the mitochondrial permeability transition in hippocampal neurons. *Journal of neuroscience research.* 1998;53(6):728-41.
10. Perkins G, Bossy-Wetzl E, Ellisman MH. New insights into mitochondrial structure during cell death. *Experimental neurology.* 2009;218(2):183-92.

11. Itoh K, Nakamura K, Iijima M, Sesaki H. Mitochondrial dynamics in neurodegeneration. *Trends in cell biology*. 2013;23(2):64-71.
12. Han X-J, Lu Y-F, Li S-A, Kaitsuka T, Sato Y, Tomizawa K, et al. CaM kinase I α -induced phosphorylation of Drp1 regulates mitochondrial morphology. *The Journal of cell biology*. 2008;182(3):573-85.
13. Cheng G, Kong Rh, Zhang Lm, Zhang Jn. Mitochondria in traumatic brain injury and mitochondrial-targeted multipotential therapeutic strategies. *British journal of pharmacology*. 2012;167(4):699-719.
14. Singh IN, Sullivan PG, Deng Y, Mbye LH, Hall ED. Time course of post-traumatic mitochondrial oxidative damage and dysfunction in a mouse model of focal traumatic brain injury: implications for neuroprotective therapy. *Journal of Cerebral Blood Flow & Metabolism*. 2006;26(11):1407-18.
15. Weber JT. Calcium homeostasis following traumatic neuronal injury. *Current neurovascular research*. 2004;1(2):151-71.
16. Young W. Role of calcium in central nervous system injuries. *Journal of neurotrauma*. 1992;9:S9-25.
17. Trump B, Berezsky I. The mechanisms of calcium-mediated cell injury and cell death [corrected]. *New horizons (Baltimore, Md)*. 1996;4(1):139-50.
18. Zhao Q, Huang, Chunhui, Li, Fuyou. Phosphorescent heavy-metal complexes for bioimaging. *Chem Soc Rev*. 2011;40(5):17.
19. Zhang ZG, Ni; Li, Ting; Mais, Dale E.; Wang, Mingwei. Quality control of cell-based high-throughput drug screening. *Acta Pharmaceutica Sinica B*. 2012;2(5):10.
20. Sierra H, Zheng J-Y, Rabin B, Boustany NN. Measurement of object structure from size-encoded images generated by optically-implemented Gabor filters. *Optics express*. 2012;20(27):28698-706.
21. Firestein, Bonnie L., et al. "Cypin: a cytosolic regulator of PSD-95 postsynaptic targeting." *Neuron* 24.3 (1999): 659-672.

CHAPTER 5

5 CONCLUSION & FUTURE DIRECTION

In this work, we have presented different approaches to detect and quantify morphological changes associated with mitochondria in three different cell-types and compared the results with a fluorescent probe. Our technique is based on optical Fourier filtering where scattered light is filtered by the hardware using Gabor filters sensitive to size and orientation. The common theme throughout the work is the assessment of mitochondrial morphology under normal and dysregulated conditions.

In Chapter 2, we used Principal Component Analysis (PCA) to reduce dimensionality and Linear Discriminant Analysis (LDA) to distinguish between apoptosis-competent and apoptosis-resistant tumor forming cells. The mutated cells, which lack Bax and Bak, scatter differently compared with those expressing Bax/Bak. Since Bax and Bak are associated with the mitochondrial membrane, the differences we observed are likely due to alterations in mitochondrial morphology. In Chapter 3, we associated the aspect ratio of mitochondria with a label-free parameter called Orientedness. We have demonstrated that Orientedness is able to report on changes in subcellular morphology in Bovine Aortic Endothelial Cells (BAEC) in response to calcium overload which causes mitochondrial rounding and/or fission. There we introduced an image analysis method to mask highly scattering organelles to discard redundant information from non- or low-scattering cytoplasm and no-cell region, thus keeping the Orientedness data pertinent to the objects of interest. While in Chapter 3 we probed changes in subcellular organelle shape, in Chapter 4 we quantified the change in

organelle size. We used a parameter called S_{\max} that encodes the size-information of the probed object. We applied S_{\max} to quantify mitochondrial dynamics such a fission, fusion etc. over time and demonstrated that this label-free parameter is capable of reporting an object's size-information even after the organelle is photo-bleached in the corresponding fluorescent channel. We also presented an alternative approach to fluorescence based kymograph to track mitochondrial dynamics and movement over time using a label-free Segmented image. Since the Segmented images do not bleach, the Kymograph generated from these images can be used to track mitochondria for longer periods of time. Another advantage of label-free kymograph is the stratified pixels that can report both organelles and processes by separate colors, which is not possible in fluorescence images.

While the above mentioned experiments and examples indicate the applicability of the light-scatter based label-free technique for tracking mitochondrial size, shape and dynamics, there is still room for improvement. For example, Non-negative Matrix Factorization (NMF) can be used to reduce dimensionality instead of PCA in Chapter 2. Unlike PCA, the basis vectors of NMF group similar features together¹. As can be seen in Figure 5-1, the physiological features contained in the W1 and W2 basis vectors of NMF represent the neuronal process shown in dark-field image better compared with the principal component PC1 obtained by PCA. This is because NMF takes the spatial relationship of the pixels in to account while clustering. Also NMF is mathematically more favorable than PCA due to the non-negative nature of the image data².

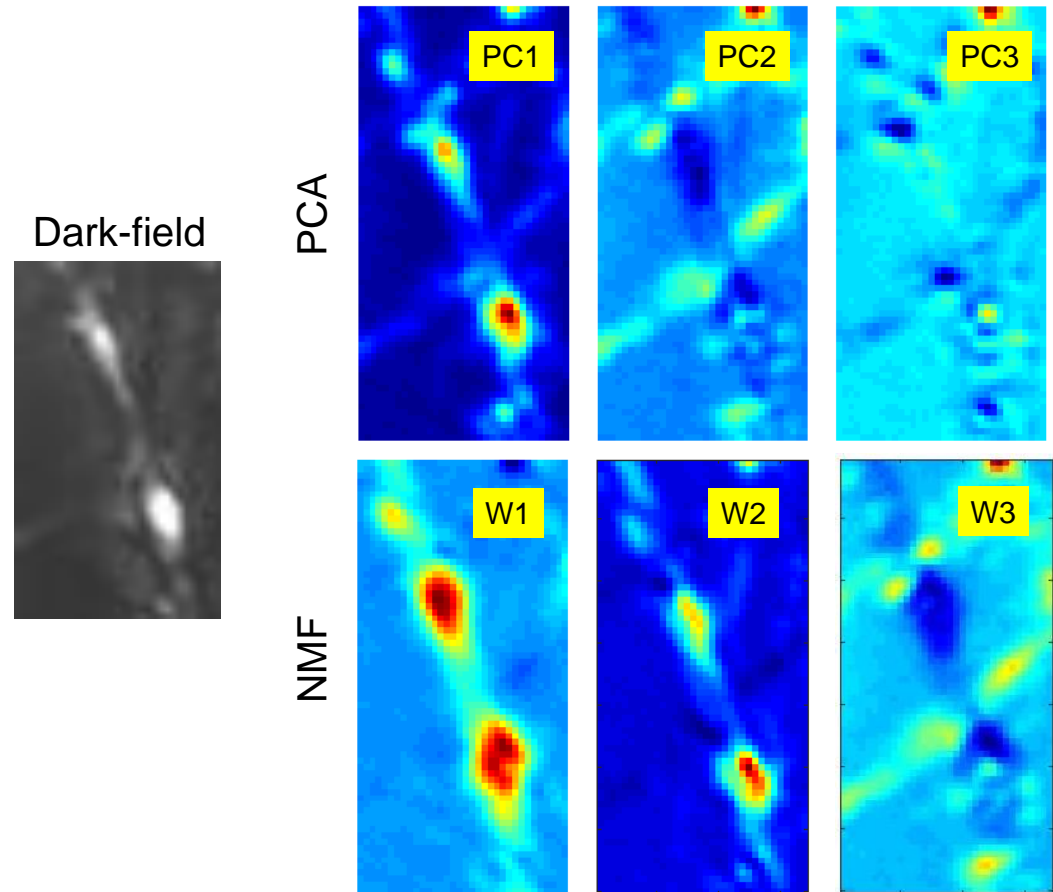


Figure 5-1 Basis functions of PCA and NMF. (top panel) principal components (PCs) of PCA and (bottom panel) basis functions of NMF contain different physiological features of a section of a neuronal processes. Note, the basis vectors of NMF (W1 and W2) contain the physiological features of the neuronal processes better compared to the PCs (PC1). Color indicates intensity of the vectors.

The edge-enhancement technique presented in Chapter 3 has limitations due to its requirement for fine-tuning input parameters based on the cell-type. Most of these parameters characterize the Log-Gabor filters used to filter the acquired images. Such dependence might be reduced by replacing the Gabor filters with Log-Gabor filters⁴ during optical filtering. In other words, instead of filtering twice – one with Gabor filters

on the hardware and subsequently with Log-Gabor filters in the digital processing step; we could filter the scattered light with Log-Gabor in the hardware and then conduct minimal processing to calculate the phase-congruency from the filtered images. Even if phase-congruency is not included in the pre-processing step, as shown in Chapter 4 for neurons, Log-Gabor filters may improve the spectral information contained in the acquired filtered images. Scattered light filtered by Log-Gabor filters is influenced by the DC component very minimally as Log-Gabor filters extinguish the DC component completely by definition³. This quality of the filtered images makes the image data invariant to the average intensity of the signal, which in turn makes it suitable for good feature generation in classification tasks⁴. Also, the bandwidth of Gabor filters is limited to one octave as a wider bandwidth will introduce high DC component. Log-Gabor filters, on the other hand, can afford to have higher bandwidth since they do not have any DC component. Thus fewer Log-Gabor filters will be required compared to Gabor filters to probe the frequency spectrum, which will greatly reduce acquisition time, hence improving time-resolution. Another improvement is achieved via the property of Log-Gabor filters that enables them to encode natural images (as opposed to cartoon or synthetic images) better. Gabor filters emphasize the low frequencies more and thus may produce redundant information⁵. Log-Gabor filters have an extended tail in the higher frequencies which makes them more suitable to probe spectral information of the natural image (i.e. scattered-light in this case), since the transfer function of Log-Gabor filter matches the power spectrum of natural images. This criterion of Log-Gabor filters might be very useful for calculating the S_{max} parameter to avoid the incorrect dominance of the lower frequencies (i.e. bigger periods).

Mitochondria play a key role in neuronal cell-death and hence there's a growing effort toward mito-protective drug discovery. To facilitate fast and reliable drug-screening, a new paradigm for the neuronal cell culture has been proposed which is commonly referred to as “brain-on-a-chip” technique⁶. Here a micro-device accommodates organotypic tissue slices and is capable to provide realistic information of the underlying biological processes in TBI. *In vitro* models for TBI such as dissociated neurons are commonly used in the labs; however, they cannot preserve the architecture of the brain and hence do not provide information regarding functional local synaptic circuitries. Brain slice models alleviate this issue by offering intact tissue-architecture as well as uninterrupted synaptic connections. Thus organotypic models are a preferred drug screening tool for neurodegenerative diseases⁷. Another advantage over commonly used neuronal culture-plates is that this device will provide a way to examine the pathophysiology of traumatic brain injury (TBI) in the tissue-context in which synaptic circuitry is intact as well as preserving some of the brain architecture. To this end, our collaborators have proposed similar devices for drug screening⁸ (Figure 5-2). It is expected that this device will provide optical, metabolic and electro-physiological assessment upon pharmacological treatment of the cultured slices.

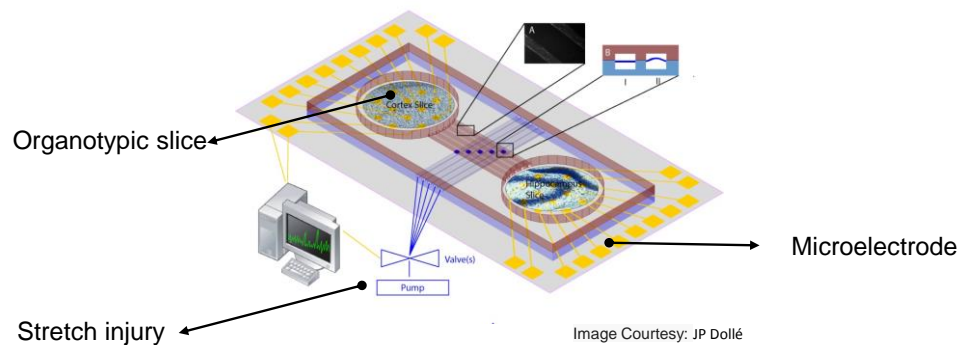


Figure 5-2 Brain-on-a-chip device. Image Courtesy: JP Dolle.

As a proof of concept, we employed one such micro-channel device⁹ to culture cortical neurons and imaged on different days in-vitro (DIV). The advantage of this particular device is that multiple devices can be fabricated and imaged together, making it a possible candidate for high-throughput applications. Figure 5-3 shows the state of the culture at different DIVs under different imaging modalities. As can be seen in the phase-contrast images (panel A & B), the processes have already started to grow through the channels by DIV 4. We have imaged again on DIV 11 and DIV 15 with fluorescence and dark-field respectively, which indicates that the device can be used to image neuronal processes over long period of time. However, the dark-field image has more background compared to the ones acquired previously. This is because the chamber containing the cell-body, channel and processes here is a well of a 96-well plate. Unlike the metal chambers employed for imaging previously, these wells are taller and contain more media, which might have interfered more with the incident light. In the future, we intend to optimize the image acquisition and apply the proposed label-free imaging techniques for possible high-throughput drug-screening.

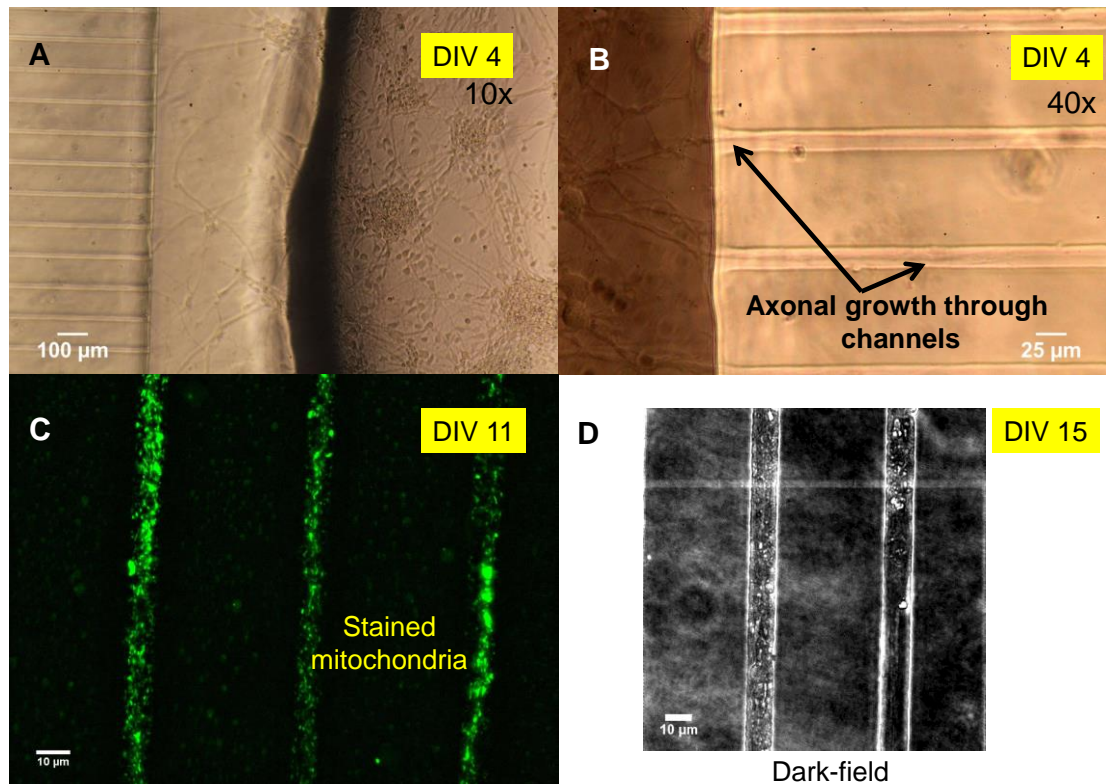


Figure 5-3 Neuronal culture in micro-device. (A, B) Phase-contrast images showing neurons in a reservoir and processes stretching through the channels (C) Fluorescent image showing mitochondrial location in the processes (D) Dark-field image showing part of two channels containing processes.

Traditional fluorescence based imaging techniques provide good localization and contrast for visualizing subcellular organelles. However, photo-bleaching, low transfection efficiency and photo-toxicity limit their applicability. Label-free techniques such as the Fourier-filtering based Optical Scatter Imaging (OSI) presented here have the ability to avoid such issues. OSI have the potential to be used for routine assessment of cellular states once the underlying biology is confirmed with fluorescence images. Specifically, the PCA approach can be used to differentiate between two populations of

cells or between pre- and post-treatment cases with different morphological properties. OSI can be used to track mitochondria in the neuronal processes as well as to probe their fusion-fission dynamics. We have also shown that this technique can reveal more information about the biological sample when compared to the fluorescent images. These features of the label-free technique may help to develop high-through screening of neuroprotective drugs in future.

References

1. Hoyer PO. Non-negative matrix factorization with sparseness constraints. *Journal of machine learning research*. 2004;5(Nov):1457-69.
2. Lee DD, Seung HS. Learning the parts of objects by non-negative matrix factorization. *Nature*. 1999;401(6755):788.
3. Field DJ. Relations between the statistics of natural images and the response properties of cortical cells. *Josa a*. 1987;4(12):2379-94.
4. Boukerroui D, Noble JA, Brady M. On the choice of band-pass quadrature filters. *Journal of Mathematical Imaging and Vision*. 2004;21(1-2):53-80.
5. Arrospe J, Salgado L. Log-Gabor filters for image-based vehicle verification. *IEEE Transactions on Image Processing*. 2013;22(6):2286-95.
6. Dauth S, Maoz BM, Sheehy SP, Hemphill MA, Murty T, Macedonia MK, et al. Neurons derived from different brain regions are inherently different in vitro: A novel multiregional brain-on-a-chip. *Journal of neurophysiology*. 2016;117(3):1320-41.
7. Cho S, Wood A, Bowlby MR. Brain slices as models for neurodegenerative disease and screening platforms to identify novel therapeutics. *Current neuropharmacology*. 2007;5(1):19-33.
8. Dollé J-P, Morrison III B, Schloss RS, Yarmush ML. An organotypic uniaxial strain model using microfluidics. *Lab on a Chip*. 2013;13(3):432-42.
9. Fantuzzo JA. *Micro-neurocircuitry: Modelling Brain Circuitry with Induced Neurons for the Study of Neuropsychiatric Disorders*: Rutgers University; 2018.